Check for updates

Advanced Optical Materials

ADVANCED OPTICAL MATERIALS
www.advopticalmat.de

RESEARCH ARTICLE

3,5-Dicyanopyridine–Phenothiazine Derivatives Exhibiting Single-Molecular White Emission for Down-Converting Electroluminescent Devices

Lesia Volyniuk[1] | Brigita Vigante[2] | Dmytro Volyniuk[1] | Nataliya M. Karaush-Karmazin[3] | Boris F. Minaev[3] | Serhii Melnykov[4] | Pavlo Stakhira[4] | Algirdas Lazauskas[5] | Sergey Belyakov[2] | Santhiya Kuppusamy[1] | Pavel Arsenyan[2] | Juozas Vidas Grazulevicius[1]

[1]Department of Polymer Chemistry and Technology, Kaunas University of Technology, Kaunas, Lithuania | [2]Latvian Institute of Organic Synthesis, Riga, Latvia | [3]Department of Chemistry and Nanomaterials Science, Bohdan Khmelnytsky National University, Cherkasy, Ukraine | [4]Department of Electronic Engineering, Lviv Polytechnic National University, Lviv, Ukraine | [5]Institute of Materials Science, Kaunas University of Technology, Kaunas, Lithuania

Correspondence: Dmytro Volyniuk (dmytro.volyniuk@ktu.lt) | Pavel Arsenyan (pavel@osi.lv) | Juozas Vidas Grazulevicius (juozas.grazulevicius@ktu.lt)

Received: 29 January 2026 | **Revised:** 15 July 2026 | **Accepted:** 10 August 2026

Keywords: 3,5-dicyanopyridine | conformer | down-converting light-emitting diode | mechanochromic luminescence | phenothiazine | single molecular white emission

ABSTRACT

3,5-Dicyanopyridine and phenothiazine derivatives exhibit attractive mechanochromic properties that enable multicolour emissions and single-molecular white emission. Large hypsochromic shifts of up to 190 nm (from red to deep blue) were observed in the developed mechanochromic compounds in response to various external stimuli. These derivatives exhibit record-breaking solid-state emission enhancement factors of up to 755, indicating that the emission intensity of their solids is substantially higher than that of solutions. Single-molecular white light emitting samples were obtained by the tuning of the substituent nature in the pyridine ring and physical approaches (different treatments of aggregate-containing liquids and solid samples). The developed compounds possess different conformational states, with emissions ranging from deep blue to red. The amorphous states exhibit single-colour emissions, while crystalline states of various packing arrangements show white or multicoloured emissions. They can be used as down-conversion white emitters in white light-emitting diodes exhibiting colour coordinates of (0.32, 0.34), (0.28, 0.30) and (0.32, 0.38), colour rendering index (CRI) of 75–78 and colour temperatures in the range from 5368 to 6668 K.

1 | Introduction

Single-molecular white-light emitters (SMWLEs) can offer significant sustainability benefits by replacing multicomponent white-light emitters in various applications. The SMWLE applications include solid-state lighting [1–4], visible light communication [5, 6], information encryption [7], sensing [8], medical research [9], and bioimaging [10]. The development of highly efficient SMWLEs can lead to decreased energy consumption, reduced greenhouse gas emissions, and minimized climate change [11]. Importantly, the synthesis of SMWLEs may requires less solvents and lower energy consumption compared to the synthesis of conventional multicomponent white-light emitters. For example, the solvent consumption for column chromatography and the energy consumption for purification by sublimation of single-molecular white-light emitters are expected to be lower than those required for the purification of multicomponent conventional emitters that yield white light. End-of-life recycling of a single white-light emitter should be simpler and/or more efficient than that of recycling multicomponent conventional white-light emitters.

All rights reserved, including rights for text and data mining and training of artificial intelligence technologies or similar technologies.
© 2026 Wiley-VCH GmbH

The conventional emitters have monochromatic blue/green/red or sky-blue/orange emissions that can produce white light in down-converting white light-emitting diodes (WLEDs) and white organic light-emitting diodes (WOLEDs) [12–14]. One of the key characteristics of organic SMWLEs is their potential to eliminate/reduce the use of expensive and/or toxic elements (such as Ir^{3+}-based emitters, cadmium or selenium-based quantum dots, or yttrium aluminium garnet doped with rare earth elements, etc.) [15, 16] which are commonly used in commercial WLEDs and WOLEDs. To utilize these advantages, some approaches have been proposed for the development of heavy-metal-free SMWLEs, including SMWLEs with dual fluorescence from different states or a combination of fluorescence and room-temperature phosphorescence (RTP) [17–20].

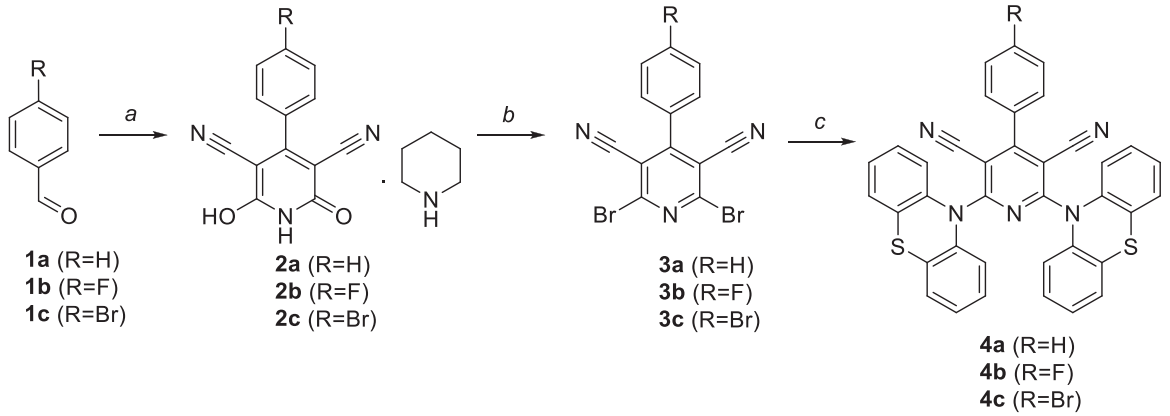
In the case of many solid-state applications, the main requirements for SMWLEs are high photoluminescent quantum yields (PLQYs) in the solid state. This can be achieved for compounds with enhanced emission in the solid state (so-called aggregation-induced emission enhancement (AIEE) effect) [21]. Despite the huge potential to increment PLQYs, there are very few reports on SMWLE materials with AIEE effect. Only a single example is mentioned in the review article on materials with AIEE published in 2022 [22]. Recently, white emission with the tuned CIE1931 coordinates from (0.29, 0.33) to (0.30, 0.36) was achieved by changing the solvent viscosity for an SMWLE with AIEE [23]. A significantly higher emission intensity was observed for the solid samples than for the solutions.

For optoelectronic applications, the ability to harness the non-emissive triplet excitons for light generation is also required. This can be implemented by exploiting organic materials that exhibit RTP [24], thermally activated delayed fluorescence (TADF) [25] or doublet emission of radicals [26]. For instance, a radical anion-forming dynamic self-assembly of photo-reduced perylene diimide demonstrated white light emission with PLQYs of 5.33 and 3.97% and CIE1931 colour coordinates of (0.33, 0.32) and (0.29, 0.27) in solutions and polymer films, respectively [27]. SMWLEs can exhibit a high-quality white RTP with CIE1931 coordinates close to those of daylight (0.33, 0.33) [28]. Their PLQY values are usually below 10%. The crystalline powder of the xanthone and diphenylamine derivatives as SMWLE showed white TADF with PLQY of 40% and the CIE1931 coordinates of (0.27, 0.35) [29]. Recently, the diindolophenthiazine derivatives were characterized by TADF with the CIE1931 coordinates of (0.31, 0.33) [30]. X. Yin et al. reported single-molecular white-light emitters for white OLEDs with EQE of 0.49% and CIE coordinates of (0.31, 0.33) [31]. Single-emitter-based OLEDs emit white electroluminescence only at 5.3 V with relatively low brightness, whereas increasing the voltage results in the shifts of the colour coordinates into the orange region. Z. Chi et al. reported single-molecular white-light emitters exhibiting both TADF and AIEE [32]. However, their applicability remains unclear. Despite the great potential of TADF/AIEE-based SMWLEs intended for the development of white-emitting optoelectronic devices, there are very few studies on these materials.

Smart organic materials that can change their emission colour under the influence of various phenomena such as mechanochromism, thermochromism, electrochromism, and photochromism are widely explored as the components of optoelectronic devices, but typically not for white-light emitting devices [33]. Many materials that change their emission colour in response to mechanical forces, known as mechanochromic materials, are characterised by a wide range of emission colours [34]. Organic MC materials are characterised by various emission phenomena, including constant or switchable TADF, RTP, or AIEE [35–37]. For example, we have recently developed mechanochromic materials with yellowish-orange TADF that can be hypsochromically shifted to blue emission by up to 92 nm under thermally controllable tuning [38]. The yellowish-orange TADF and the blue fluorescence result from the relaxation of charge transfer (CT) states of two different conformers of the donor-acceptor-type compounds. It is predictable that these compounds can emit white light when their different emission colours overlap. However, white emission has not been observed in a similar way to many other mechanochromic emitters under different external treatments [39, 40]. Over the last 10 years, we have been working on the idea of developing a pure organic SMWLE that exhibits improved TADF in the solid-state with mechanochromic properties. To achieve the desired chromaticity coordinates of equal-energy white (0.333, 0.333), we have studied numerous scaffolds, but the most promising ones were 3,5-dicyanopyridines. For example, a series of 4-carbazolylphenyl-substituted, symmetrical and unsymmetrical 3,5-dicyanopyridines showed deep-blue to yellow emissions with PLQYs of up to 98% for oxygen-free toluene solutions [41]. Carbazole- or phenothiazine-containing dicyanopyridines substituted with multiple donors exhibited green or orange TADFs, which enabled the fabrication of highly efficient single-colour OLEDs with external quantum efficiencies of up to 25% [42]. The electron-transporting materials with 3,5-dicyanopyridine acceptor moiety were used as hosts in OLEDs and showed considerably better performance (EQE of 21.9%) than that (EQE of 12.4%) of the conventional host 3,3′-di(9*H*-carbazol-9-yl)-1,1′-biphenyl [43]. Having successful examples, we have chosen 3,5-dicyanopyridine core and decorated it with phenothiazine moieties, resulting in donor-acceptor-donor-type compounds. Both moieties were previously exploited for the development of single-color AIEE and TADF emitters [41, 44]. The phenothiazine moiety was selected in part for its ability to form two distinct conformers ("quasi-equatorial" (q-e) and "quasi-axial" (q-a)) that can cause mechanochromic luminescence [46–48].

Herein, we report results confirming that phenothiazine-decorated 3,5-dicyanopyridines exhibit pronounced dual charge transfer emission, mechanochromic luminescence tunability, and solid-state-enhanced emission. This property is characterized by the shift of the emission colour between red and deep blue, which corresponds to a shift of the emission spectrum by up to 190 nm. To the best of our knowledge, such shifts are rather exceptional for organic mechanochromic materials. The synthesized compounds exhibit TADF and AIEE. Using different approaches, high-quality white emissions can be achieved from the aggregate-containing liquids, powders, and films of the newly designed 3,5-dicyanopyridines. This work provides deep insights into the conversion of emitters with mechanochromic luminescence into highly effective SMWLEs. The potential applications of developed SMWLEs were demonstrated by studying white down-conversion light-emitting diodes with a single emitter. Those devices emit white light with colour

21951071, 2026, 35, Downloaded from https://advanced.onlinelibrary.wiley.com/doi/10.1002/adom.71715 by Dmytro Volyniuk - Kaunas University Of Technology , Wiley Online Library on [03/11/2026]. See the Terms and Conditions (https://onlinelibrary.wiley.com/terms-and-conditions) on Wiley Online Library for rules of use; OA articles are governed by the applicable Creative Commons License



SCHEME 1 | Preparation of 2,6-di(10*H*-phenothiazin-10-yl)-4-arylpyridine-3,5-dicarbonitriles **4a–c**. *Reaction conditions: (a): cyanoacetamide, MeOH, piperidine, heating; (b): $POBr_3$, 170°C, 1 h; c: 10H-phenothiazine, NaH, 60°C, overnight*.

coordinates (0.32, 0.34), (0.28, 0.30) and (0.32, 0.38), colour rendering index (CRI) of 75–78 and colour temperatures in the range from 5368 to 6668 K.

2 | Results and Discussion

2.1 | Synthesis

The target compounds were prepared according to Scheme 1. Necessary piperidinium 3,5-diciano-6-hydroxy-4-(4-substituted phenyl)pyridin-2-olates **1** and appropriate 2,6-dibromo-4-(4-substituted phenyl)-pyridine-3,5-dicarbonitriles **2** were obtained by the previously published methods [41, 42]. Further introduction of 10*H*-phenothiazine groups in position 2 and 6 of 2,6-dibromides **3a–c** using sodium hydride as base resulted in the corresponding 2,6-di(10*H*-phenothiazin-10-yl) substituted 3,5-dicarbonitriles **4a–c** in good yields.

2.2 | X-Ray Analysis of Single Crystals

The molecular structures of derivatives **4b** and **4c** were clearly confirmed by X-ray analysis at different temperatures from 150 to 363K (Figure 1). It was found that the crystals of **4b** and **4c** are characterized by considerable thermal expansion. We link variations in geometric characteristics to variations in emissions as discussed below. For **4b**, the average volumetric coefficient of thermal expansion (α_V) in the temperature range from −123°C to +90°C is $1.408 \cdot 10^{-4}$ K^{-1}. The average value of α_V for **4c**, in the temperature range from −113°C to 0°C is $1.391 \cdot 10^{-4}$ K^{-1}. This slight difference in the thermal expansion can be explained by the replacement of F by Br in **4c**. The larger bromine atomic radius affects the overall crystal packing density and flexibility. Table 1 represents the main crystal data and structure refinement parameters for **4b** and **4c** estimated at the different temperatures. Figure 1A–D shows a perspective view of molecules **4b** and **4c** with thermal ellipsoids (displacement ellipsoids are drawn at the 50% probability level) and the atom-numbering scheme followed in the text. The crystal structures of **4b** and **4c** are isomorphous. Crystal structures of **4b** and **4c** show dynamic behaviour to temperature changes due to the nature of their intermolecular interactions (π-hole interactions, CH···N, and CH···F or CH···Br hydrogen bonding interactions).

For compounds **4b** and **4c**, 1,4-thiazine rings have a characteristic boat conformation ("quasi-axial" [40]). In molecule **4b**, the aromatic pyridine ring is not strictly planar but has a flattened twist conformation. At 150 K, the deviations of atoms from the least-squares plane of the pyridine ring are as follows: 0.016(1), −0.087(2), 0.060(2), 0.021(2), −0.080(2), and 0.053(2) Å for N1, C2, C3, C4, C5, and C6 atoms, respectively. This flattened twist conformation is also preserved at higher temperatures and occurs for the crystals **4c**. This fact indicates that the nonplanar pyridine ring is not a consequence of packing effects but is a consequence of congestion in the molecular structures of **4b** and **4c**. The significant packing effects are indicated by deviations of the C23, C26, and F29 (or Br29) atoms from the line of atoms N1, and C4. In a perfectly symmetrical molecular structure with the point symmetry group C_2, these atoms should lie on the N1, C4 line, but due to packing effects and congestion in the molecular structure, the atoms deviate significantly from this line. Table 1 lists deviations of these atoms from the N1, C4 line.

The main feature of the **4b** crystal structure estimated at 150 K is the presence of a strong intermolecular π-hole interaction between the S39 atom of one molecule and the pyridine ring of another. The distance between the sulphur atom and the centroid of the pyridine ring is 3.284(2) Å; the shortest atom-atomic contact of this interaction is S39···N1(1−*x*, 2−*y*, 1−*z*) with a length of 3.229(1) Å. By means of these strong interactions, molecules of **4b** associate into centrosymmetric dimers in the crystal structure. Intermolecular atom-atomic contacts C18···F29(1½−*x*, ½+*y*, 1½−*z*) and C16···N22(2−*x*, 1−*y*, 1−*z*) can be considered as weak hydrogen bonds of the CH···F and CH···N types, respectively. The molecular packing in the crystal structure with these π-hole interactions and hydrogen bonds is shown in Figure 1C. With increasing temperature, all these intermolecular contacts weaken significantly since the thermal vibrations increase at elevated temperatures, which leads to bond stretching and reduces the strength of non-covalent interactions. This is a typical case for crystal structures. Table 1 shows how these interactions

21951071, 2026, 35, Downloaded from https://advanced.onlinelibrary.wiley.com/doi/10.1002/adom.71715 by Dmytro Volyniuk - Kaunas University Of Technology , Wiley Online Library on [03/11/2026]. See the Terms and Conditions (https://onlinelibrary.wiley.com/terms-and-conditions) on Wiley Online Library for rules of use; OA articles are governed by the applicable Creative Commons License

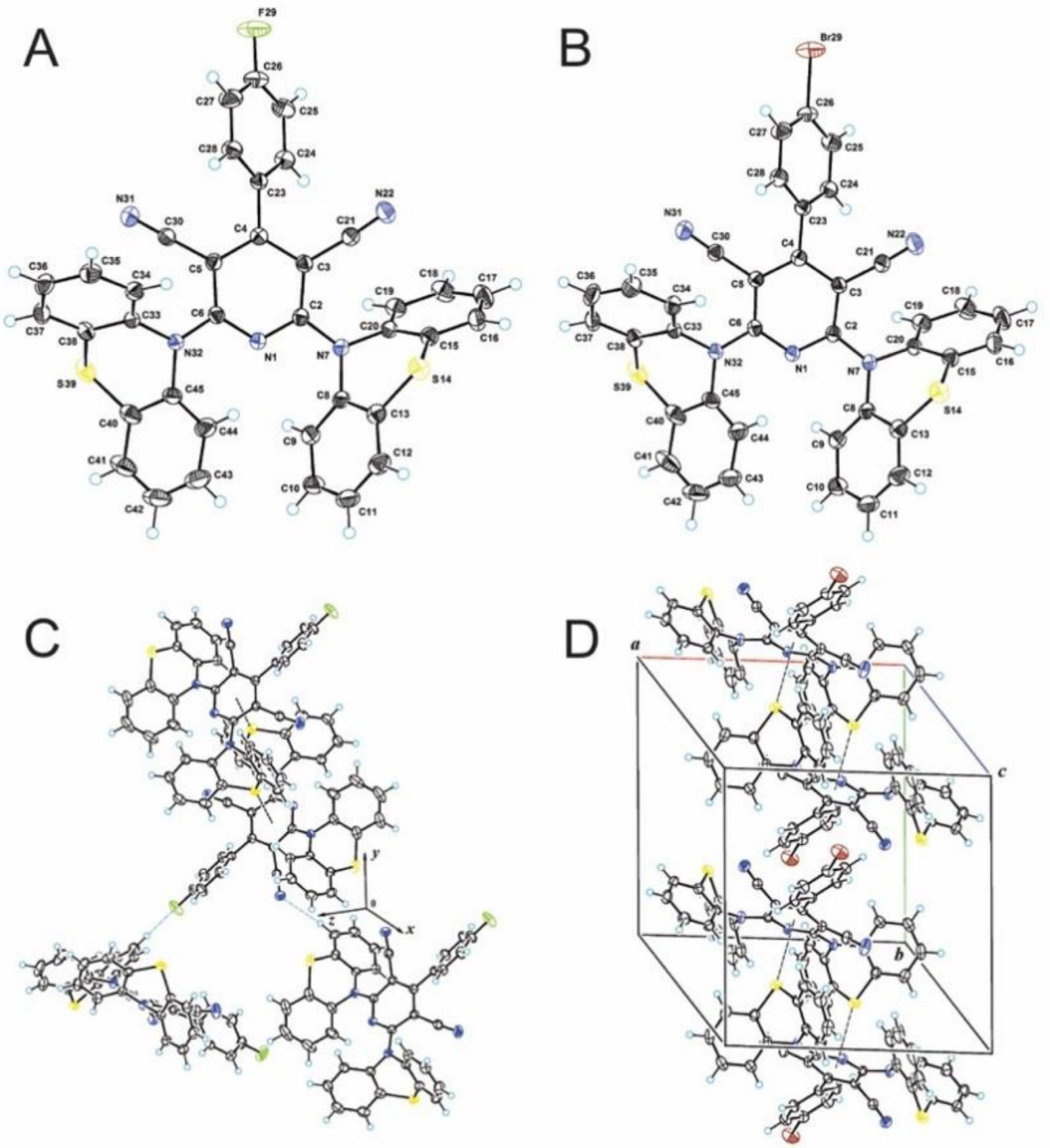


FIGURE 1 | Oak ridge thermal ellipsoid plots with the labels of atoms for molecular structures of **4b** at 150 K (A) and **4c** at 160 K (B); a fragment of molecular packing in the crystal structure of **4b** showing π-hole interactions and hydrogen bonds (C); unit cell contents in the crystal structure of **4c** (dashed lines show π-hole interactions) (D).

change with increasing temperature. Since the crystal structure of **4c** is isomorphic to the structure of **4b**, all the described intermolecular interactions are also characteristic for **4c**, except for the fact that instead of a fluorine atom F29, it contains a bromine atom (Br29). The inclusion of a large bromine atom (Br29) somewhat weakens the intermolecular interactions in **4c** due to steric effects and less efficient hydrogen bond overlap. Changes in these interactions are shown in Table 1. Figure 1D represents the packing of molecule **4c** in a unit cell. Moreover, we compared the molecular conformations in the crystal state with the energy-minimised conformations obtained through time-dependent density functional theory (TDDFT) optimisation as discussed below (Section 2.3.5).

2.3 | Photophysical Properties and Theoretical Model of Absorption and Emission Changes

2.3.1 | DFT/TDDFT Investigation of Conformer-Dependent Absorption, Emission, and Excited-State Properties

The absorption and photoluminescence (PL) spectra of dilute toluene and tetrahydrofuran (THF) solutions ($\sim 10^{-5}$ M) as well as films are summarised in Figure 2A,B. Compounds **4a**–**c** showed the absorption peak (λ_{abs}) at 320 nm, two shoulders at 360 and 378 nm, and a low-intensity tail at wavelengths above 400 nm. To explain the absorption character of **4a**–**c**, we

21951071, 2026, 35, Downloaded from https://advanced.onlinelibrary.wiley.com/doi/10.1002/adom.71715 by Dmytro Volyniuk - Kaunas University Of Technology , Wiley Online Library on [03/11/2026]. See the Terms and Conditions (https://onlinelibrary.wiley.com/terms-and-conditions) on Wiley Online Library for rules of use; OA articles are governed by the applicable Creative Commons License

TABLE 1 | Geometric characteristics of the crystal structures **4b** and **4c** estimated at the different temperatures.

Characteristic	4b			4c	
	at 150 K	at 273 K	at 363 K	at 160 K	at 273 K
Atomic deviation from the line of N1, C4 atoms:					
*Δ*C23/Å	0.091(2)	0.091(2)	0.080(2)	0.137(3)	0.124(5)
*Δ*C26/Å	0.370(2)	0.370(2)	0.313(4)	0.551(3)	0.514(7)
*Δ*F29/Å	0.521(2)	0.521(2)	0.441(3)	—	—
*Δ*Br29/Å	—	—	—	0.873(2)	0.814(2)
S39⋯C_s [a)]/Å	3.284(2)	3.338(2)	3.378(2)	3.243(2)	3.315(4)
S39⋯N1/Å	3.229(1)	3.258(2)	3.283(2)	3.288(2)	3.314(3)
C18⋯F29 (or Br29)/Å	3.261(3)	3.324(3)	3.377(3)	3.596(2)	3.643(3)
H18⋯F29 (or Br29)/Å	2.56(2)	2.63	2.69	2.89(3)	2.97
C18–H18⋯F29 (or Br29)/°	130(2)	128	131	131(4)	129
C16⋯N22/Å	3.528(3)	3.580(3)	3.623(4)	3.439(3)	3.477(5)
H16⋯N22/Å	2.59(2)	2.64	2.71	2.52	2.58
C16–H16⋯N22/°	171(2)	170	169	163	162

[a]C_s is centroid of the pyridine ring (N1, C2, C3, C4, C5, C6).

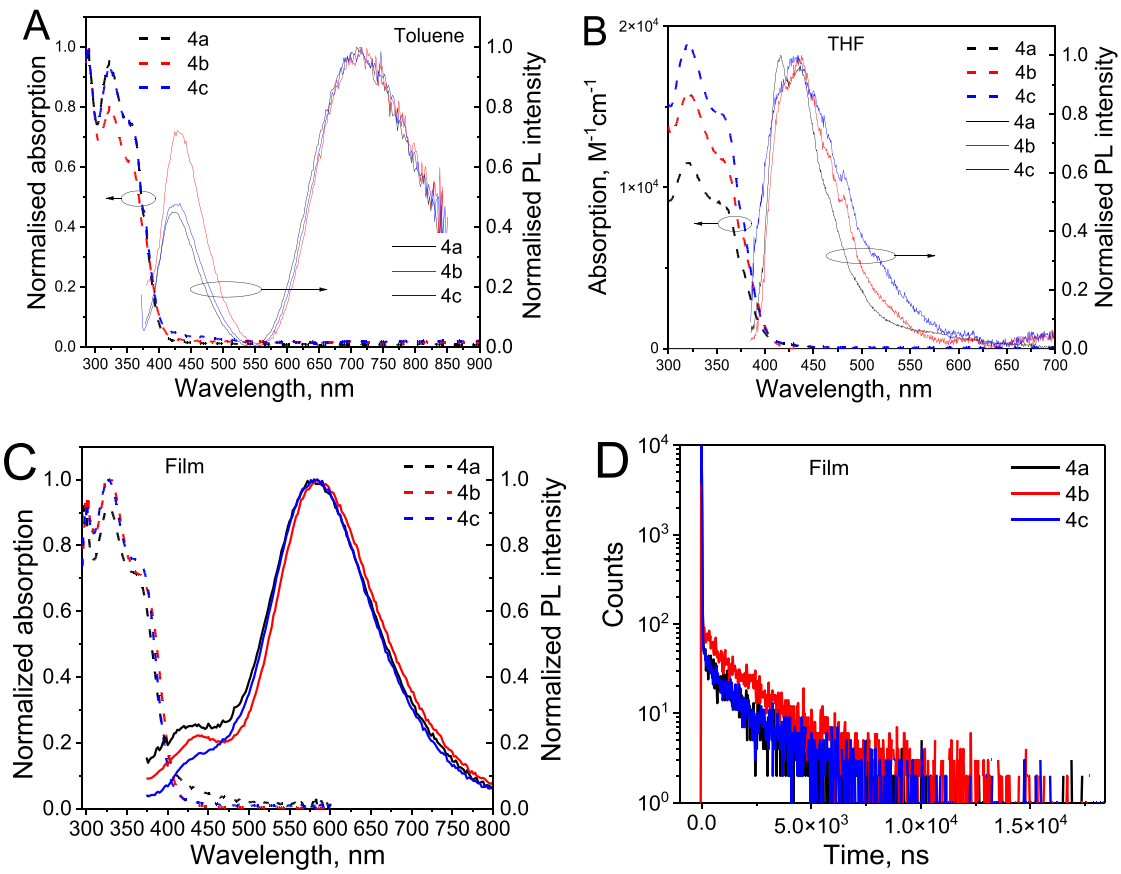


FIGURE 2 | Absorption and emission spectra of toluene (A) and THF (B) solutions and films (C) of **4a–c**. PL decay curves (D) of films of **4a–c** collected at 580 nm using laser excitation at 374 nm.

21951071, 2026, 35, Downloaded from https://advanced.onlinelibrary.wiley.com/doi/10.1002/adom.71715 by Dmytro Volyniuk - Kaunas University Of Technology , Wiley Online Library on [03/11/2026]. See the Terms and Conditions (https://onlinelibrary.wiley.com/terms-and-conditions) on Wiley Online Library for rules of use; OA articles are governed by the applicable Creative Commons License

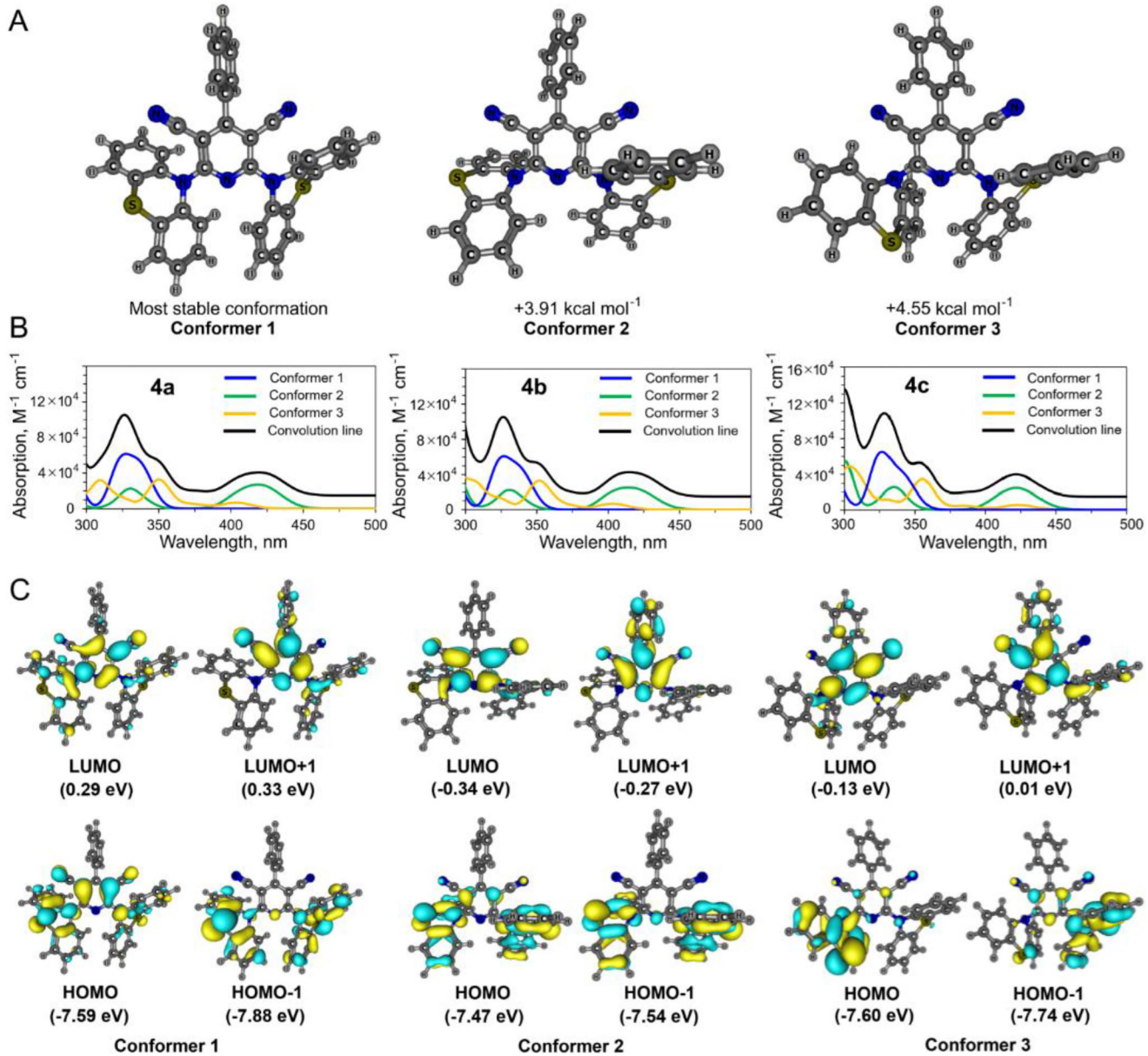


FIGURE 3 | DFT/wB97XD/6-31G(d,p) calculated structures of three conformers 1–3 for **4a** with the corresponding energy differences relative to the most stable conformer 1 (A), TDDFT simulated absorption spectra of **4a–c** obtained taking into account the THF effects (B), and molecular orbitals of **4a** in the ground S_0 state (C). HOMO represents the highest occupied molecular orbital, and LUMO is the lowest unoccupied molecular orbital. The black line in the absorption spectra corresponds to the convolution profile of all the simulated spectra.

modelled three structural conformers for each molecule using the DFT/wB97XD/6-31G(d,p) method (Figure 3A and Table S1). The main structural difference between these conformers lies in the spatial orientation of the phenothiazine fragments (Table S2). Conformer 1 represents the most sterically stable conformation for **4a–c**, as it was confirmed by X-ray analysis (Figure S1). The other two conformations 2 and 3 are higher in energy (Table S1). For **4a**, the energy differences are 3.91 and 4.55 kcal mol^{-1} for conformers 1 and 2, respectively, relative to the most stable configuration (Figure 3A). This means that conformer 1 is the dominant form for **4a–c**, while the higher-energy conformers 2 and 3 are less populated, but still present and may contribute to the overall properties, especially in solutions where multiple conformers 1–3 can coexist and affect the absorption and emission spectra. TDDFT computations reproduced the experimentally observed low-intensity tail for **4a–c** calculated in the 400–430 nm range (Figure 3B and Table S3). This tail is mainly due to weakly allowed CT-dominated transitions into the S_1, S_2, S_3, and S_4 states in conformer 2, and transitions to the S_1 state in conformer 3 (Figure 3B). These transitions correspond to the combination of HOMO-1→LUMO, HOMO→LUMO, HOMO→LUMO+1, and HOMO-1→LUMO+1 configurations in conformer 2, and the HOMO→LUMO configuration in conformer 3 (Figure 3C and Tables S3–S6). The involved molecular orbitals (MOs) for conformers 1 and 2 are partially spatially separated between the donor-localized occupied MOs and the acceptor-centered unoccupied MOs, which reduces the transition energy and explains the red-shifted, broad, weak absorption in the range

21951071, 2026, 35, Downloaded from https://advanced.onlinelibrary.wiley.com/doi/10.1002/adom.71715 by Dmytro Volyniuk - Kaunas University Of Technology , Wiley Online Library on [03/11/2026]. See the Terms and Conditions (https://onlinelibrary.wiley.com/terms-and-conditions) on Wiley Online Library for rules of use; OA articles are governed by the applicable Creative Commons License

of 400–430 nm. This absorption results from CT-dominated transitions with a mixed local-excited (LE)/CT character in which the electron density is transferred from the phenothiazine donor fragments to the 3,5-dicyanopyridine acceptor moiety. The experimentally observed two shoulders at 360 and 378 nm can be mostly attributed to the second absorption band in conformer 3 (Figure 3B). For example, for conformer 3 of **3a** the shoulder at 378 nm is associated with the calculated $S_0 \rightarrow S_2$ and $S_0 \rightarrow S_3$ transitions at 379 and 374 nm, respectively, while the shoulder at 360 nm corresponds to the calculated $S_0 \rightarrow S_4$ transition at 350 nm (Tables S3 and S4). The transitions into the S_2 and S_3 states exhibit the same orbital nature. Both correspond to the combination of HOMO-1→LUMO and HOMO→LUMO+1 configurations with different wave function contributions. The transition to the S_4 state is due to the HOMO-1→LUMO+1 configuration (Figure 3C). For **4b** and **4c**, the two shoulders are also attributed to the absorption of conformer 3, whose electronic nature is similar to that of conformer 3 of **4a** (Tables S3–S6).

The absorption band observed at 320 nm corresponds to the calculated absorption of the most stable conformer 1 for compounds **4a**–**c** with the maxima at 326 nm for **4a**, 327 nm for **4b**, and 330 nm for **4c** (convolution line in Figure 3B). This absorption band has a complex nature due to transitions into S_1, S_2, S_3, and S_4 states in conformer 3 of **4a**–**c**. The first $S_0 \rightarrow S_1$ transition in conformer 1 corresponds to the HOMO→LUMO configuration, while the $S_0 \rightarrow S_2$, $S_0 \rightarrow S_3$, and $S_0 \rightarrow S_4$ transitions are attributed to HOMO→LUMO+1, HOMO-1→LUMO, and HOMO-1→LUMO+1 configurations with different wavefunction contributions (Figure 3C and Tables S3–S6). The increment of molar absorption coefficients (ε) at 320 nm was in the order of 1.15×10^4 $M^{-1}cm^{-1}$ for **4a**, 1.56×10^4 $M^{-1}cm^{-1}$ for **4b**, and 1.88×10^4 $M^{-1}cm^{-1}$ for **4c** (Figure 2B and Table 2). The TDDFT calculations overestimate the ε values because of limitations of the computational model, but reproduce the general tendency of a slight increase in ε values for conformer 1 moving from **4a** to **4c**. Thus, the atoms of H, F, or Br slightly affect ε values of **4a–c** but do not visibly change their absorption wavelengths. The presence of F and Br slightly modulates the electronic structure of **4b** and **4c** by changing the electron density distribution and molecular orbital energy levels (Figure 3C). This results in the increase of the electric transition dipole moment, which in turn increases ε.

Minor changes in the absorption and emission wavelengths are observed across the series **4a**–**c**, while the ΔE_{ST} remain within a relatively narrow range (0.35–0.42 eV experimentally; Table 2). The slightly larger ΔE_{ST} value observed for **4c** suggests that the bromine substituent influences the relative stabilization of the singlet and triplet excited states through its electronic effect and increased polarizability.

The LUMO+1 and HOMO-1 energies are close to LUMO and HOMO, respectively (Figure 3C and Tables S3–S6). This means that higher-order transitions also contribute to the observed spectra, especially for conformers 2 and 3. The absorption spectra of toluene solutions are similar to those of THF solutions, except for the intensity of the tails observed at wavelengths longer than 400 nm (Figure S7). The polarity of the solvent influences the CT-dominated transitions responsible for absorption above 400 nm. The nonpolar toluene provides less stabilization of the excited charge-separated states, thus increasing the intensity of these transitions in the absorption spectra. This effect is more pronounced for the fluoro-substituted **4b**. The presence of the strong electronegative fluorine atom in **4b** lowers the LUMO energy level (acceptor orbitals) more than the HOMO energy level (donor orbitals), making the CT from the donor to the acceptor more energetically favourable. In the nonpolar toluene environment, this enhanced CT interaction is more noticeable because the solvent does not hinder or mask it. At first glance, the absorption spectra of doping-free films and of the films of the molecular dispersions in a polymer were similar (Figure 2C and Figure S8). However, the intensity of the tail at wavelengths longer than 400 nm is stronger for films, which can be due to the stronger contribution of conformer 2, which is supported for the three conformers of **4a** by the results of TDDFT calculations (Figure 3).

The peaks of PL spectra of THF solutions were observed in the range of 416–436 nm (Figure 2B and Figure S7 and Table 2). In contrast, most of the studied solutions, including the toluene solution (Figure 2A), exhibit dual CT emissions (Figure S7). High- and low-energy bands at 416–436 nm and at wavelengths longer than 600 nm were observed, respectively. These results are in good agreement with the dual CT emissions of previously published 3,5-dicyanopyridine-containing multiple donor moieties [42].

TDDFT/wB97XD/6-31G(d,p) calculations accounting for THF solvent effects indicate that the observed broad-range emission in the range of 416–436 nm results from the formation of multiple conformers in solution, which contribute to the overall emission spectra. For example, the experimental emission observed at 416 and 437 nm (Table 2) for compound **4a** corresponds to the vertical $S_1 \rightarrow S_0$ transition calculated for the two spatial conformers at 525 and 533 nm (Table S7). These bands experience red shifts compared to the experimental emission, which is a typical overestimation for CT transitions within TDDFT calculations. The TDDFT/wB97XD/6-31G(d,p) calculations performed for THF solutions indicate a small energy difference (0.03 kcal mol^{-1}, Figure S2) between conformers 1 and 2 of **4a** in the excited S_1 state, i.e., these conformers are almost isoenergetic and can be populated almost equally in the S_1 state (Figure 4). Conformer 1 represents the most stable configuration. These conformers differ in the orientation of the benzene fragment to the right (conformer 1) or the left (conformer 2) relative to the 3,5-dicyanopyridine core and phenothiazine fragments (Figure S2). Both conformers are stabilized with intramolecular CH···N interactions with distances of 3.307 and 3.337 Å for conformer 1 and of 3.295 and 3.375 Å for conformer 2 (Figure S2). Compounds **4b** and **4c** show larger energy differences between their conformers 1 and 2 (0.10 and 0.07 kcal mol^{-1} for **4b** and **4c**, respectively, Figure S2), resulting in a more selective population of conformers in the S_1 state and narrower individual contributions to the emission spectra. However, the overall PL spectra of **4b** and **4c** remain to be broadened by conformational diversity. The CT character of the emission of all the conformers is evident due to the significant spatial distribution of their MOs (HOMO, LUMO, etc., Figure S3). The partial spatial overlap between the donor-localized occupied MOs and the acceptor-centered LUMO indicates a mixed LE–CT character rather than a purely CT excitation, consistent with the experimentally observed relatively large ΔE_{ST} values (0.35–0.42 eV, Table 2). This indicates that efficient TADF is unlikely in the solution-phase conformations, which supports the idea

21951071, 2026, 35, Downloaded from https://advanced.onlinelibrary.wiley.com/doi/10.1002/adom.71715 by Dmytro Volyniuk - Kaunas University Of Technology , Wiley Online Library on [03/11/2026]. See the Terms and Conditions (https://onlinelibrary.wiley.com/terms-and-conditions) on Wiley Online Library for rules of use; OA articles are governed by the applicable Creative Commons License

TABLE 2 | Thermal and photophysical characteristics of compounds **4a–c**.

Compound	Sample	4a	4b	4c
$T_c/T_m/T_{5\%}$, °C	Powder	216/332/391	232/315/422	290/350/404
CIE 1931 (*i*/*g*), (x, y)		(0.245, 0.232)/(0.419, 0.394)	(0.222, 0.199)/(0.355, 0.326)	(0.333, 0.292)/(0.495, 0.461)
λ_{abs}, nm / ε, $M^{-1}cm^{-1}$	THF solution	320/1.15×10^4	320/1.58×10^4	320/1.89×10^4
λ_{em}, nm / $\Delta\upsilon$, cm^{-1}		416, 437/7212	436/8314	432/8102
$S_1/T_1/\Delta E_{ST}$, eV		3.2/2.82/0.38	3.14/2.79/0.35	3.23/2.81/0.42
CIE 1931 (f_w of 70%), (x, y) [a]	DMF/water	(0.411, 0.457)/(0.290, 0.281)	(0.428, 0.472)/(0.288, 0.297)	(0.443, 0.467)/(0.287, 0.375)
I/I_0 (f_w of 90%)		100/115	461/555	530/755
λ_{em}, [b] nm	Neat film	586	586	586
PLQY, %		9.6	5.8	8.8
PLQY, % (f_w of 90%)	DMF/water [e]	6.2	4.8	5.4
PLQY, % (f_w of 90%)	DMF/water [f]	8.4	7.6	8.6
λ_{em}, [c] nm	1 wt.% Zeonex solution dispersions	575	575	575
PLQY, %		12.9	10.6	12.2
λ_{em}, [d] nm	1 wt.% Zeonex powder dispersions	435, 560	435, 542	459, 563
PLQY, %		15.7	9.7	18

[a]before and after thermal annealing.
[b]taken from PL spectra collected in Figure 2c.
[c]taken from PL spectra collected in Figure S8.
[d]taken from PL spectra collected in Figure S28.
[e]Before thermal annealing.
[f]After thermal annealing.

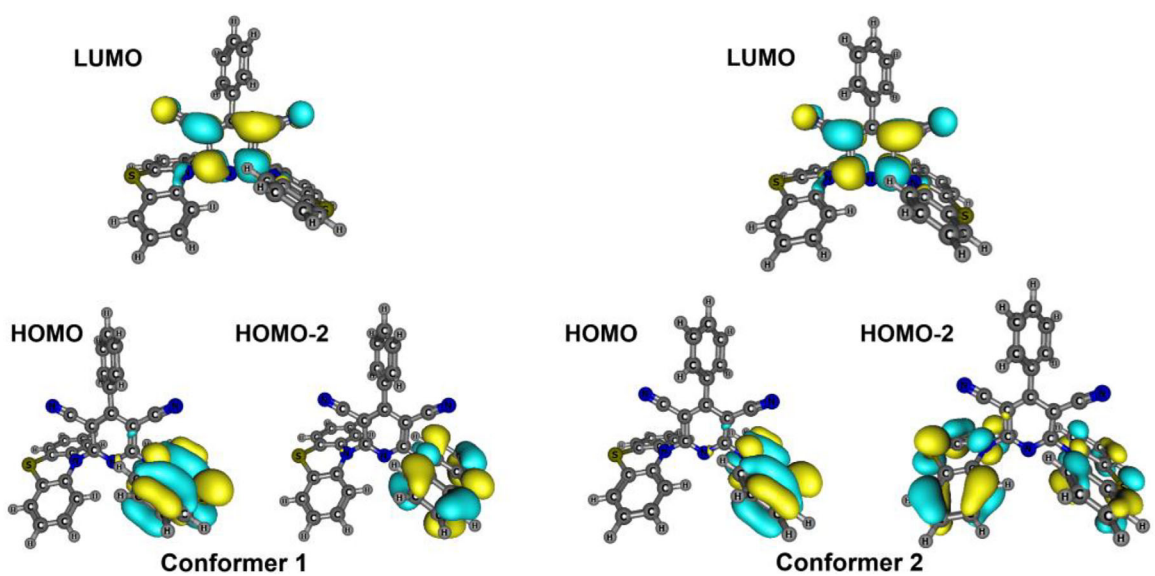


FIGURE 4 | Molecular orbitals of the excited S_1 state of the conformers 1 and 2 of **4a**. (yellow and blue colours mean positive and negative signs of wave functions).

that delayed emission arises predominantly from a solid-state conformational confinement. The emission of **4a** is determined by the combination of LUMO→HOMO and LUMO→HOMO-2 configurations in both conformers 1 and 2 (Figure 4). This corresponds to CT from the 3,5-dicyanopyridine accepting core (LUMO) to the phenothiazine donor fragments (HOMO and HOMO-2). The main difference in the CT of conformers 1 and 2 is that in the case of conformer 2, both phenothiazine fragments are involved in CT, while for conformer 1, only one of the phenothiazine fragments participates in the CT (Figure 4). This

21951071, 2026, 35, Downloaded from https://advanced.onlinelibrary.wiley.com/doi/10.1002/adom.71715 by Dmytro Volyniuk - Kaunas University Of Technology , Wiley Online Library on [03/11/2026]. See the Terms and Conditions (https://onlinelibrary.wiley.com/terms-and-conditions) on Wiley Online Library for rules of use; OA articles are governed by the applicable Creative Commons License

means that the CT is more delocalized in conformer 2, leading to the more efficient CT. PL of **4b** and **4c** has the same CT-dominated nature (Figure S3). The main trend in the calculated TDDFT PL spectra is a slight red shift from **4a** to **4b** (Table 2 and Table S7). This observation is consistent with the experimentally observed trend, indicating that the calculations qualitatively capture the relative electronic properties and conformational effects of **4a** and **4b**.

The optimized S_1 state of conformer 2 has a total energy 0.54 eV lower than that obtained by the vertical absorption calculations (Table S1). Thus, we easily predict a large Stocks shift for the PL peak. In the region of 416–436 nm, the low-intensity PL bands were observed for the layers of doping-free **4a** and of polymer-hosted **4a**. The most intense PL bands peaking at 585 nm were observed for the doping-free films, and at a close wavelength of 580 nm for the films of the molecularly doped polymer. This observation indicates that the environment does not strongly influence the PL peak position of the solid samples. The Stokes shifts ($\Delta\upsilon$) of THF solutions ranged from 7212 to 8314 cm^{-1} (Table 2). The large Stokes shifts confirm the substantial relaxation of the molecules between the absorption and emission processes, with significant geometry reorganization occurring in the excited state (Figure S1) before the emission.

The PL and phosphorescence (with 0.1 ms delay) spectra of dilute THF solutions of **4a–c** were recorded at low temperature (77 K) to study the energy levels of the lowest excited singlet and triplet states (S_1 and T_1) (Figure 5A). Taking the determined energies of S_1 and T_1 states, the energy gaps (ΔE_{ST}) were found to be 0.38 eV for **4a**, 0.35 eV for **4b**, and 0.42 eV for **4c** (Table 2). Such ΔE_{ST} values are generally considered too large to enable efficient TADF. The experimental ΔE_{ST} values reported here were obtained exclusively from the low-temperature THF solution data, whereas the most direct evidence for small ΔE_{ST} relevant to TADF originates from the thin-film measurements. The solution-phase and solid-state ΔE_{ST} values reflect different molecular conformations, packing environments, and degrees of structural relaxation.

The DFT/wB97XD/6-31g(d,p) calculated adiabatic ΔE_{ST} values were estimated to be 0.17 eV for **4a**, 0.16 eV for **4b**, and 0.19 eV for **4c** (Table S7). The significant difference between the experimental and calculated ΔE_{ST} values in TADF systems is attributed to the well-known limitations of conventional TDDFT in accurately describing CT excited states and electron correlation effects. The larger ΔE_{ST} of **4c** compared to the corresponding values of **4a** and **4b** can be explained by the electronic influence of the Br substituent on the excited-state electronic structure. The presence of Br is expected to enhance spin-orbit coupling (SOC), thereby facilitating intersystem crossing (ISC). Nevertheless, the **4a–c** films exhibited TADF-like delayed fluorescence behaviour in the solid state (Figure 2D), although a full mechanistic confirmation across all environments was not performed. We studied the photophysical properties of the compounds at different temperatures (Figure 5B,C and Figure S9). These data support the TADF of **4a–c**. It should be noted that the shapes of PL spectra are similar at the different temperatures. The change in temperature to 77K does not affect the shape of PL spectra, since the phosphorescence band is closely located to that of fluorescence. This is typical for TADF compounds with small single-triplet energy splitting. The photoluminescence intensity increases upon oxygen removal (Figure S10). The TADF of compounds **4a–c** can be explained by molecular packing features and intermolecular interactions in the solid state, which facilitate charge transfer, leading to a lower ΔE_{ST} value and effective TADF.

The DFT/ωB97XD/6-31G(d,p) dimer calculations for 4b indicate that crystal packing induces conformational confinement and intermolecular electronic coupling, resulting in increased configurational mixing and enhanced intermolecular CT character in the lowest excited states. These effects are expected to reduce the exchange interaction responsible for singlet-triplet splitting and therefore provide a plausible microscopic explanation for the substantially smaller ΔE_{ST} observed experimentally in the solid film compared with isolated molecules in solution. The more detailed discussion is provided in the Supporting Information (Section IV). Taken together, the temperature-dependent PL spectra and PL decay measurements of the **4b** films support this interpretation. A very small ΔE_{ST} value of 0.03 eV, determined from the low-temperature fluorescence and phosphorescence spectra of the film (Figure 5D), is fully consistent with efficient reverse intersystem crossing and the observed TADF behaviour.

2.3.2 | Mechanochromic Luminescence

To support the above predictions, we investigated the mechanochromic luminescence properties of powders **4a–c**. White emission was observed in the powders of the synthesized compounds upon UV excitation (Figure 6A). The photoluminescence (PL) spectra of the initial powders of compounds **4a–c** showed two bands at 425/550, 434/567, and 435/622 nm, respectively (Figure 6B). CIE 1931 colour coordinates of the emission of the powders, solutions, and films of **4a–c** can be tuned in a wide range, approaching the natural white colour with CIE 1931 (0.33, 0.33) (Figure S11 and Tables S8–S11). The PL bands were characterised by either prompt or delayed fluorescence of different conformers of **4a–c** (Figure 6C and Figure S12). The decay curves of prompt fluorescence are characterised by two to three components (τ_1-τ_3), while decay curves of delayed fluorescence can be represented by single exponential functions which disclose the lifetimes τ_3 or τ_4 (Table S12). These data are in good agreement with the multi-colour emission of **4a–c** (Tables S8–S11).

White emissions of the initial powders of **4a–c** exhibited high sensitivity to external stimuli. Upon exposure to mechanical stress or melting, the samples of **4a–c** displayed orange emissions (Figure 6A). The melting process was performed at the melting temperatures (T_m) of 332°C for **4a**, 315°C for **4b**, and 350°C for **4c** taken by differential scanning calorimetry (DSC) measurements (Table 2 and Figure S13). Thermogravimetric analysis (TGA) revealed high thermal stabilities of compounds **4a–c**, with 5% mass loss temperatures ($T_{5\%}$) of 391°C, 422°C, and 404°C, respectively (Table 2 and Figure S14).

The changes in the emissions of **4a–c** after the different treatments can be explained by the differences in molecular packing in the solid state, driven by structural/conformational changes.

21951071, 2026, 35, Downloaded from https://advanced.onlinelibrary.wiley.com/doi/10.1002/adom.71715 by Dmytro Volyniuk - Kaunas University Of Technology , Wiley Online Library on [03/11/2026]. See the Terms and Conditions (https://onlinelibrary.wiley.com/terms-and-conditions) on Wiley Online Library for rules of use; OA articles are governed by the applicable Creative Commons License

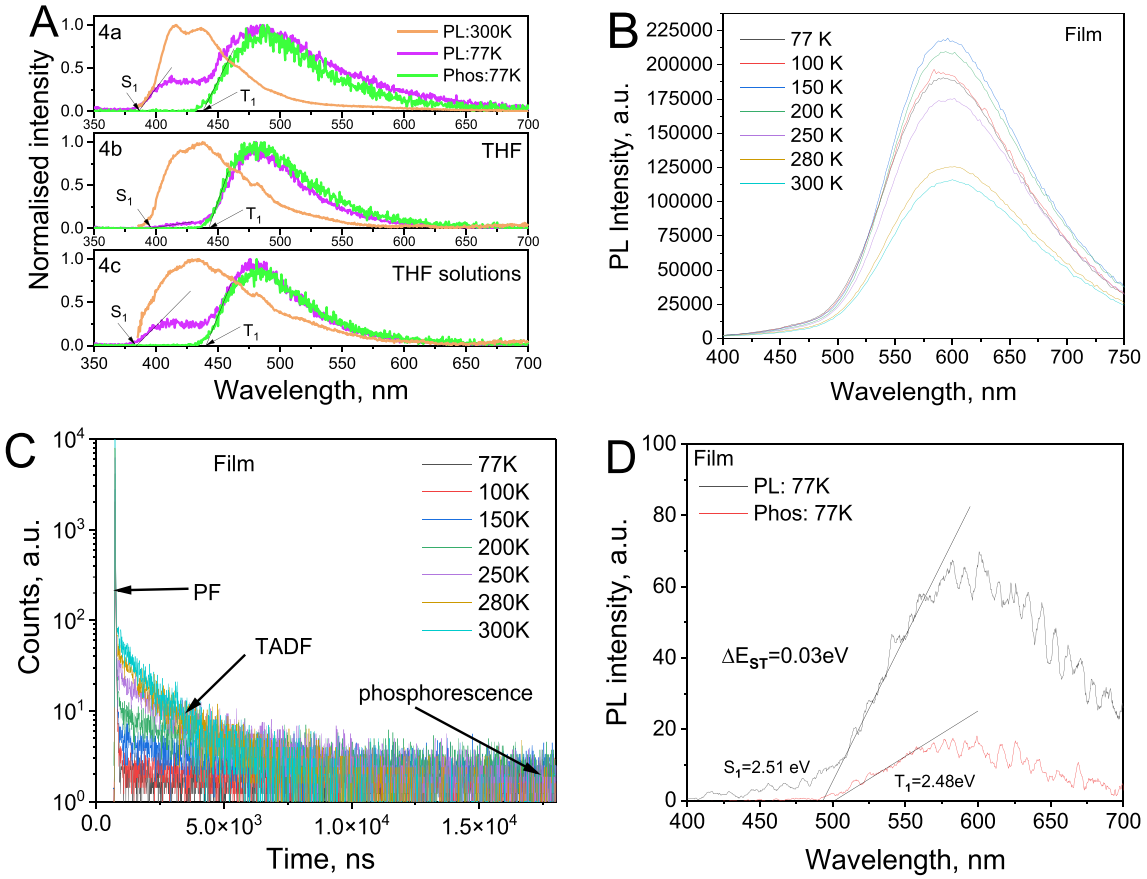


FIGURE 5 | PL and phosphorescence (Phos.) spectra (A) of THF solutions. PL spectra (B) and PL decay curves (C) for the film of **4b** recorded at the different temperatures. PL and phosphorescence (Phos) spectra (D) for the film of **4b** at 77K.

This prediction perfectly agrees with theoretical results based on the density functional theory (DFT) calculations and structural optimizations (Table S1). The following data can be used for the explanation of the properties of the synthesized compounds exhibiting mechanochromic luminescence of the studied compounds [49]. The initial powders are characterised by certain degrees of crystallinity, with degrees of crystallinity measured at 25% for **4a**, 42.5% for **4b,** and 27.4% for **4c** (Figure 6D). In contrast, the grinding rendered the samples completely amorphous. Their emissions are primarily attributed to one conformer emitting in the orange spectral region with PL intensity maxima at 593 nm for **4a**, 600 nm for **4b**, and 606 nm for **4c**, respectively (Figure 6B). Notably, the melted samples displayed similar PL spectra, suggesting comparable molecular arrangements after melting.

The molecular packing of **4b–c** was adjusted by treating the grounded samples in saturated vapours of toluene. The fumed samples of **4b–c** demonstrated white, bluish-white, and orangish-white emissions, respectively (Figure 6A). X-ray diffractograms of the fumed samples revealed that the molecular packing is related either to crystallisation or to molecular arrangements toward the most stable conformers (Figure 6D). For instance, the fumed sample of **4c** was characterized by a crystallinity of 29.5% (Figure 6D). Meanwhile, the samples of **4a** and **4b** were still amorphous after toluene fuming. The fumed sample of **4c** showed whitish-orange emission with an unstructured broad fluorescence spectrum featuring two bands at 445 and 586 nm. The fumed samples of **4a** and **4b** emitted in the deep-blue region. PL spectra and PL decay curves of the heated samples were additionally investigated. The heating (thermal annealing) of the samples of **4b** and **4c** was carried out for 10 min at temperatures slightly higher than their crystallization temperatures (T_c) of 216°C for **4a**, 232°C for **4b**, and 290°C for **4c** (Table 2 and Figure S14). The annealed sample of **4c** showed greenish-white emission. The PL spectrum had an intensity peak at 494 nm and a shoulder at 428 nm. The PL spectrum with the peaks at 462 and 554 nm was recorded for the annealed sample of **4b**. These observations suggest that the derivative of phenothiazine and 3,5-dicyanopyridine can adopt at least three stable conformers with very different emissions. The overlapping of the emissions of the different conformers results in white emission. To support this hypothesis, time-resolved emission spectroscopy (TRES) measurements were performed for the initial powders of **4a–c** using laser excitation at 374 nm (Figure 7A and Figure S15). These measurements allow the separation of the emission spectra of different conformers based on their distinct lifetimes. The time-resolved PL spectra of the initial powders of **4a–c** were collected in the time range of 500 ns (Figure 7A and Figure S15B,C). These spectra were characterised by three bands marked as C1, C2, and C3. The intensity and position of these bands (C1–C3) varied over time after excitation, reflecting

21951071, 2026, 35, Downloaded from https://advanced.onlinelibrary.wiley.com/doi/10.1002/adom.71715 by Dmytro Volyniuk - Kaunas University Of Technology , Wiley Online Library on [03/11/2026]. See the Terms and Conditions (https://onlinelibrary.wiley.com/terms-and-conditions) on Wiley Online Library for rules of use; OA articles are governed by the applicable Creative Commons License

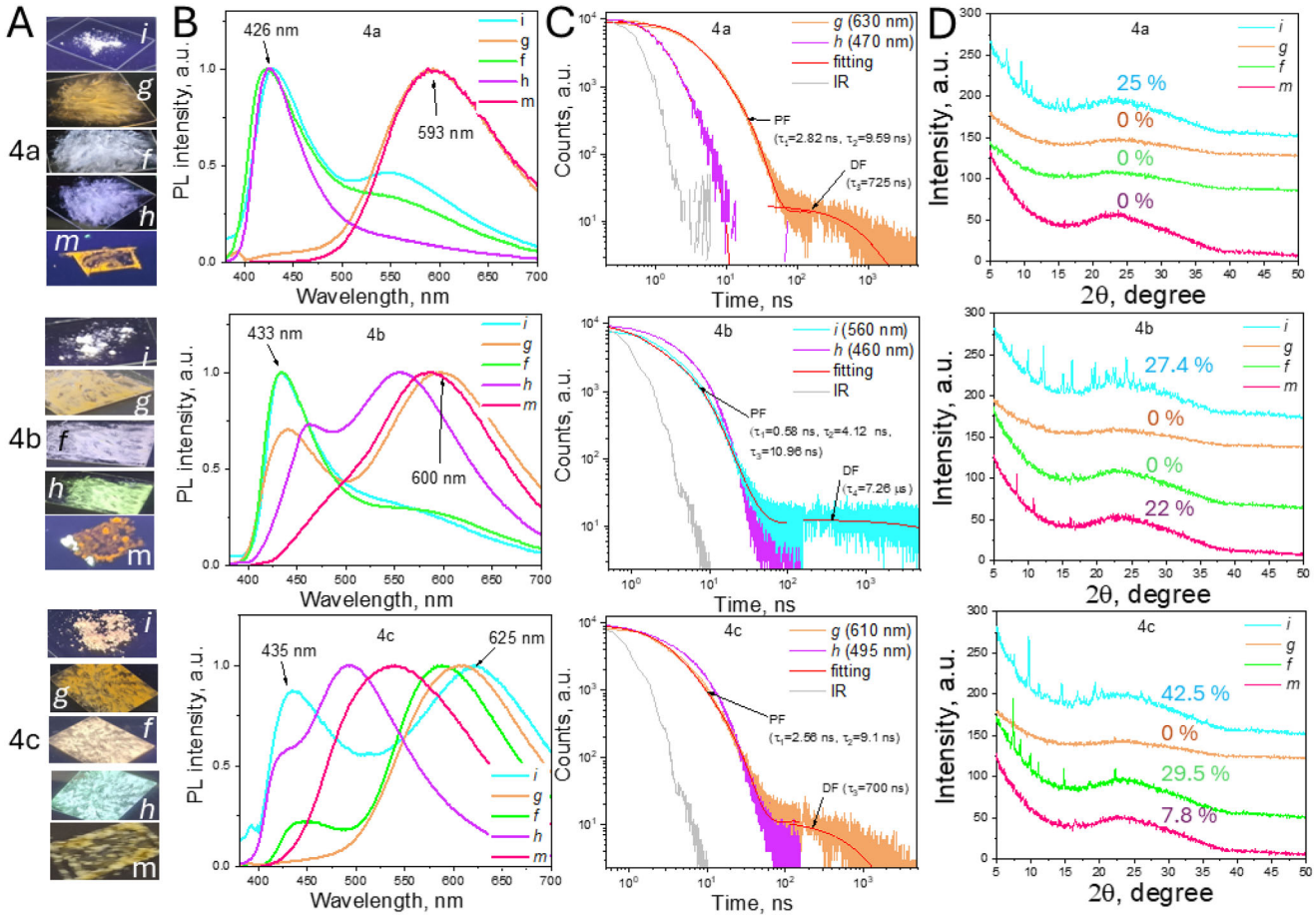


FIGURE 6 | Pictures (A), PL spectra (B), PL decay curves (C) and X-ray diffractograms (D) of the differently treated samples of **4b–c** (*i* – initial, *g*-grinded, *m*-melted, *f*-fumed, *h*-heated). PL decay curves were recorded at the wavelengths shown in the brackets.

strong conformational disorder and the structural inhomogeneity of the initial powders of **4a–c**. All three PL bands reflected prompt and delayed fluorescence (schematically marked as PF and DF in Figures 5c and 6c and Figure S16). The most intense DF was observed for the band C3, which for powder **4b** was observed in the range of 560–598 nm during the measurement time intervals of 0–500 ns. This spectral diversity resulted in significant variation of the lifetime of the CT emissions and the corresponding CIE 1931 colour coordinates of the initial powders of **4a–c**. Remarkably, these coordinates were close to the natural white color point, with CIE 1931 values of (0.33, 0.33) (Figure S11).

2.3.3 | Effects of Aggregation on Emission Intensity and Colour

To study whether white emission can be obtained for **4a–c**, we recorded PL spectra of their dispersions in dimethylformamide (DMF)/water mixtures with the different volume ratios of DMF and water (Figure 7B and Figure S17). These measurements also allowed us to investigate the AIEE properties of **4a–c**. We did not select THF/H_2O mixtures because we performed the thermal treatment of the liquid mixtures. Thus, we selected DMF with a high boiling point of 153°C. The dispersions of **4a–c** in DMF/water mixtures were thermally treated in an ultrasonic bath at a temperature of ca. 80°C. To demonstrate the effects of aggregate formations in DMF/water mixtures and their temperature treatments on emission intensities, the ratios (I/I_0) of the integrated PL intensity (I_0) of the solution in the good solvent DMF to the integrated PL intensity (I) of the solid aggregate-containing dispersions in DMF/water mixtures were estimated by the formula:

$$\frac{I}{I_0} = \frac{\int \Phi(\lambda)\, d\lambda}{\int \Phi_0(\lambda)\, d\lambda}$$

The log values of I/I_0 as a function of water fraction (f_w) in DMF/water mixtures are plotted in Figure 7B and Figure S17A. These ratios might also be considered as solid-state emission enhancement factors. The unit of the I/I_0 value is naturally seen at a f_w value of zero (Figure S18). Increasing f_w values can result in a decrease in the I/I_0 value and bathochromic shifts in CT emissions caused by the increasing polarity of DMF/water mixtures with higher water content. This was observed for the dispersion of **4a** in DMF/water mixtures of **4a** at f_w of 10%. The SSE values are below unity for organic emitters that exhibit aggregation-induced quenching. The increase in f_w can also lead to an increase in I/I_0 values caused by AIEE. This was observed for the dispersions of **4a-4c** in DMF/water mixtures at f_w higher than 10% (Figure 7B and Figure S17A). The highest I/I_0 values of 100, 461, and 530 were observed for the dispersions of **4a–c** with a f_w of 90% (Table 2). Thus, compound **4c** was characterized by

21951071, 2026, 35, Downloaded from https://advanced.onlinelibrary.wiley.com/doi/10.1002/adom.71715 by Dmytro Volyniuk - Kaunas University Of Technology , Wiley Online Library on [03/11/2026]. See the Terms and Conditions (https://onlinelibrary.wiley.com/terms-and-conditions) on Wiley Online Library for rules of use; OA articles are governed by the applicable Creative Commons License

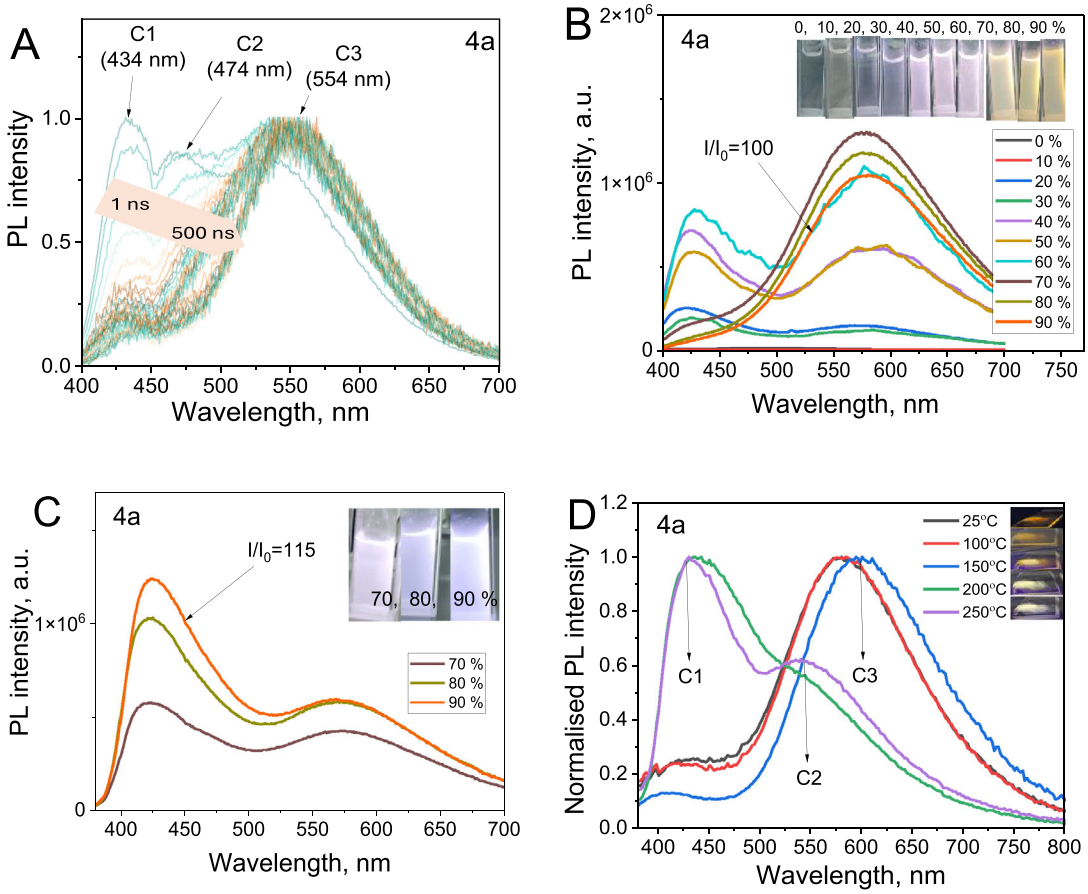


FIGURE 7 | Time-resolved PL spectra of **4a** obtained by slicing of TRES data by steps of 1 ns in the region of 0–24 ns and by steps of 25 ns in the region of 25–500 ns (A). PL spectra of the dispersions of **4a** in DMF/water mixtures before (B) and after (C) annealing at 80°C. Insets show photos of the samples under UV excitation. I/I_0 values are given for the water fraction of 90%. PL spectra (D) of the films of **4a** annealed at the different temperatures. The inset shows the corresponding photos of the samples.

the most distinct AIEE, which could cause the best bioimaging contrast when compound **4c** is used for such an application [50]. All three compounds showed whitish emissions when dispersed in DMF/water mixtures with f_w below 70%. At f_w values of 70%, 80%, and 90%, the dispersions of **4a–c** in DMF/water mixtures were characterised by orange emissions similar to the emissions of their amorphous grinded powders (Figure 6A). Considering the relatively high boiling points of the selected solvents, we adjusted the orange emissions of **4a–c** to whitish emissions by heating the dispersions at 80°C for 10 min (Figure 7C and Figure S17B). With such an approach, the CIE 1931 colour coordinates of the emission of the dispersions of **4a–c** in DMF/water mixtures can be tuned in a wide range, approaching those of the natural white colour with CIE 1931 (0.33, 0.33) (Figure S19 and Tables S7 and S8). Emission colour matching of dispersions of organic emitters in miscible mixtures has been observed previously [51]. SMWLEs were observed using miscible solvent mixtures of water and THF [52]. To the best of our knowledge, the tuning of the emission of the dispersion of a single emitter in a miscible solvent mixture to the white has not been reported so far. Heating of the dispersion of **4a** in a DMF/water mixture at 80°C allowed a complete conversion of orange emission to the white one (Figure 7C). It should be noted that the treatment of the dispersions of **4a–c** in DMF/water mixtures with f_w values of 90% at 80°C helped us to additionally improve I/I_0 values to 115, 555, and 755, respectively (Figure 7C and Figures S17B and S18). This also results in PLQY increments for DMF/water mixtures with f_w values of 90% before and after thermal treatments at 80°C (Table 2). PL intensities of dispersion of the compounds in a DMF/water mixture do not decrease significantly after UV treatment, suggesting relatively good photostability (Figure S20). Compounds **4a** and **4c** are more promising for optoelectronic applications in terms of stability because their dispersions in a DMF/water mixture showed better photostability than **4b**. However, PL intensities of **4a–c** (1 wt.%) in Zeonex polymer-based films are more sensitive to UV and thermal treatment (Figure S21). This observation relates to issues of photostability and thermal stability of Zeonex, which show a decrease in transparency under UV and thermal treatment (Figure S22). Relatively stable devices containing compounds **4a–c** may be obtained by choosing stable hosts that are resistant to UV and heat.

2.3.4 | Effect of Thermal Annealing of Films on Their Photophysical Properties

Taking into account that the white emissions of powders or dispersions are of less practical interest than those of the films, we studied the photophysical properties of the films of **4a–c** after

21951071, 2026, 35, Downloaded from https://advanced.onlinelibrary.wiley.com/doi/10.1002/adom.71715 by Dmytro Volyniuk - Kaunas University Of Technology , Wiley Online Library on [03/11/2026]. See the Terms and Conditions (https://onlinelibrary.wiley.com/terms-and-conditions) on Wiley Online Library for rules of use; OA articles are governed by the applicable Creative Commons License

different thermal treatments (Figure 7D and Figure S23). At elevated temperatures, films of **4a–c** do not exhibit any orange emission observed at room temperature. Bands C1-C3 could be detected in the PL spectra of the films recorded after thermal annealing (Figure 7D and Figure S20). The appearance of the bands is in very good agreement with the results of the TRES measurements. They can be attributed to three different conformations of compounds **4a–c** (Figure 7A and Figure S15). The differences in the emission properties of the same films can be explained by the different geometric orientations of the molecules and the interactions within the untreated and treated films. The CIE 1931 colour coordinates of the emissions of the films of **4a–c** are given in Figure S19 and Table S11. These colour coordinates are also not far from (0.33, 0.33), demonstrating that the films of **4a–c** with white emission can be obtained if either the deposition conditions or the treatment procedures are well optimized. This assumption is supported below by the white-emitting optoelectronic devices with the single-component emitting layers of **4a–c**. Meanwhile, the reasons for the white emission of **4a–c** are investigated in detail by additional experimental and theoretical approaches.

As it is demonstrated above, the wide tuning of emission colours of powders, dispersions and films **4a–c** suggests a controllable approach to white light. These exceptional emission properties of **4a–c** are not only related to the q-e and q-a conformations of phenothiazine [40], but also to the non-planar conformations of the acceptor, as it is discussed below.

2.3.5 | Conformational Effects and Their Influence on Emission in Solution and Solid State

Three conformers were modelled for each compound (**4a**–**c**), which reflects the rotational freedom around key C–C and C–N bonds (Figure 3A and Tables S1 and S2). They differ from each other by the spatial orientation of the phenothiazine fragments relative to the 3,5-dicyanopyridine core. The differences in the conformers 1–3 of **4a**–**c** result in slightly different bond lengths and angles and have an impact on electronic distribution and interactions within the molecules. For all compounds in the series **4a**–**c**, conformer 1 corresponds to the global minimum on the potential energy surface. The higher stability of conformer 1 arises from a favourable balance of steric interactions and donor-acceptor alignment, which leads to a more uniform bonding pattern across the molecule. Conformers 2 and 3 of **4a**–**c** exhibit more significant bond length variations, which correspond to slightly higher energy states (they are higher in energy by 3.91–5.02 kcal mol^{-1}, Table S1), making them thermally less favourable. The optimized structures and bond lengths for all the modelled conformers 1–3 of **4a**–**4c** are presented in Table S2. The main structural peculiarities across all the series for each configuration include relatively consistent C—C bond lengths in the aromatic rings of ca. 1.390 Å (Table S2). This means that the aromatic cores are structurally rigid. The C—N bond lengths show the most pronounced structural differences for conformers 1–3 of **4a**–**c** (Table S2), which affect the electron density distribution and orbital interactions, influencing electronic transitions. The C—S bond lengths also exhibit slight variations in the range of 1.76–1.79 Å for conformers 1–3 of **4a**–**c** (Table S2), which contribute to the rigidity of the overall structures and help to maintain conformational stability. Conformers 2 and 3 of **4a**–**c** demonstrate the most variations in bond lengths that lead to the broadened or shifted absorption peaks due to increased electron density variability. Compound **4c** shows the greatest structural flexibility, which can result in the most significant spectral shifts compared to **4a** and **4b** (Figure 3B), as discussed above.

We should also highlight that the observation of a higher-energy emission in the crystalline state compared to the amorphous state is atypical for aggregated systems and should be carefully considered. We attribute this behaviour mainly to conformational effects imposed by crystal packing, rather than to conventional aggregation-induced red shifts. The phenothiazine units exhibit a nonplanar, butterfly-like geometry, which arises from the presence of the sulfur atom. This makes these structures sensitive to intermolecular interactions and packing constraints in the solid state. In the crystalline phase, such interactions can restrict intramolecular rotations and enforce a more rigid molecular conformation. Such conformational locking reduces structural relaxation in the excited state. It can suppress low-energy emissive pathways, which leads to a blueshifted (higher-energy) emission relative to the amorphous state, where a broader distribution of conformers is available.

To study this effect in more detail, we compared the molecular conformations observed in the single-crystal X-ray structure (at 273 K) of **4b** with the energy-minimized conformer 1 for **4b** and **4c** obtained from DFT/ωB97XD/6-31G(d,p) optimization (Figure S1). The molecular conformation of **4b** and **4c** in the solid state closely resembles the lowest energy conformer 1 of **4b** and **4c**, respectively, obtained from DFT data, with only minor differences in bond lengths and dihedral angles. In particular, for the aromatic framework of **4b** and **4c**, the C—C bond lengths in the phenyl, pyridine, and phenothiazine rings remain almost unchanged. In the X-ray structure of **4b** (Figure S1A), these bonds are in a narrow range of approximately 1.37–1.40 Å, while the DFT-optimized structure (Figure S1B) shows very similar values, which differ by no more than 0.01–0.02 Å. This confirms that the π-conjugated backbone is structurally rigid and largely unaffected by crystal packing or computational relaxation. Slightly larger differences are found for the C—N bonds connecting the phenothiazine donors to the dicyanopyridine core. In the crystal structure, these bonds are somewhat shorter (by ∼0.02–0.03 Å, Figure S1A) compared to the DFT-optimized geometry. This can be explained by intermolecular interactions and packing forces in the crystal, which tend to enhance donor-acceptor electronic coupling. For **4b**, the C—S bond lengths within the phenothiazine units are also very similar in both structures, lying in the range of 1.77–1.78 Å in the X-ray structure and 1.78–1.79 Å in the DFT-optimized geometry (Figure S1). These small differences indicate that the butterfly-like geometry of the phenothiazine moiety is well preserved after optimization. Moderate differences appear in the dihedral angles, which describe the relative orientation of the phenothiazine units with respect to the acceptor core. In the crystal structure, these dihedral angles are slightly smaller (by about 3°–7°) than those obtained from DFT optimization, which reflects a somewhat more planar donor-acceptor arrangement enforced by crystal packing. In contrast, the DFT-optimized structure allows slightly larger torsional freedom, consistent with relaxation in the absence of explicit intermolecular constraints. Similar structural peculiarities were found for **4c** (Figure S1C,D).

21951071, 2026, 35, Downloaded from https://advanced.onlinelibrary.wiley.com/doi/10.1002/adom.71715 by Dmytro Volyniuk - Kaunas University Of Technology , Wiley Online Library on [03/11/2026]. See the Terms and Conditions (https://onlinelibrary.wiley.com/terms-and-conditions) on Wiley Online Library for rules of use; OA articles are governed by the applicable Creative Commons License

Such agreement between X-ray structure and DFT-optimized geometry indicates that crystal packing stabilizes a geometry that is close to the global minimum on the potential energy surface and suppresses access to higher-energy and more distorted conformations. These higher-energy conformations are associated with improved CT character and lower emission energies.

The interpretation of the conformational locking is fully consistent with the thermal and photophysical parameters summarized in Table 2. In solution, compounds **4a**–**c** exhibit long-wavelength emission, which is characteristic of relaxed excited states with pronounced CT character. These red-shifted emissions correlate with relatively broad spectral profiles in Figure 2A,B and reflect the presence of multiple conformers with varying donor-acceptor torsion angles, as discussed above. In contrast, in the solid film state, the emission maxima shift significantly to shorter wavelengths (ca. 580–610 nm, Figure 2C), which indicates suppression of excited-state structural relaxation and reduced CT stabilisation, in agreement with conformational constraints.

This trend is further supported by the relatively low emission intensity listed in Table 2. The relatively low emission intensity in solution (notably in THF, Table 2) compared to that in the film is consistent with enhanced nonradiative decay pathways associated with conformational freedom. After film formation, partial conformational restriction reduces internal conversion and stabilizes a narrower emissive manifold, which leads to improved radiative decay efficiency and spectrally narrower emission observed experimentally. This behaviour is reflected in the blue-shifted photoluminescence observed experimentally in the solid state or high-water-fraction mixtures.

Another observation is that the measured singlet-triplet energy gaps (ΔE_{ST} = 0.35–0.42 eV, Table 2) remain relatively large across the series, indicating that the emissive states retain partial local-excited character rather than being purely CT in nature. This observation supports the conclusion that the higher-energy emission in the solid state does not arise from excimer or strongly aggregated states, which typically exhibit smaller ΔE_{ST} values and red-shifted emission. Instead, the data are consistent with emission from a more rigid, less CT-dominated conformation stabilised in the solid state.

2.4 | Single Emitter-Based Down-Converting Light-Emitting Diodes

For the illustration of the potential application of single-molecular white-light emitters, white light-emitting diodes based on single emitters were fabricated for down-conversion. Commercial ultraviolet LEDs were coated with down-converting white-emitting films of **4a**–**c**, dispersed in an inert cyclo-olefin polymer matrix (Zeonex), thereby fabricating devices A, B, and C, respectively. These UV LEDs were selected because they emit at the absorption edges of **4a**–**c**. Zeonex is transparent in the near-UV and visible regions [53]. In the absence of the white-emitting films for down-conversion, the commercial UV LED emits light peaking at 396 nm (Figure S24). With the light-emitting layer, devices A, B and C were characterised by broad emission spectra, with only a weak band at 396 nm attributable to UV LEDs (Figure 8A–C). The emission spectra of devices A, B, and C have peaks in the deep blue region at 414, 429, and 401 nm, and peaks in the yellowish region at 543 nm, 531 nm (shoulder), and 552 nm, respectively (Figure S25). The position of these bands is in good agreement with those of the PL spectra of **4a**–**c** in different media. The emission spectra of devices A, B and C are similar in shape across the different applied voltages. As a result, the emission colour coordinates of devices A, B, and C remained stable across different applied voltages (Figure 8D and Table S13). The colour coordinates of the white emissions of devices A, B, and C are close to those of daylight (0.33, 0.33). Devices A, B, and C demonstrated similar colour rendering indices (CRI) of 75–78 and slightly different colour temperatures in the range from 5368 to 6668 K (Figure S26 and Table S14). The current (CE), power (PE), and external quantum efficiencies (EQE) of the white-emitting devices were in the ranges of 4.2–10.3 cd/A, 4.4–10.8 lm W^{-1}, and 2.2%–2.8%, respectively (Table S14). Voltage-current curves of devices A–C, attributable to UV LEDs. The white light-emitting diodes show different brightness because different down-converting emitters **4a–c** were used (Figure S27). The results show that it is feasible to produce white devices with a single down-converting emitter. Unlike conventional white LEDs and OLEDs, single-molecular white emitters could lessen environmental effects, as their synthesis requires fewer solvents compared to that of conventional multicomponent white emitters.

To place the performance of the present systems in the context of recently reported SMWLEs, a comparative analysis of recent representative literature examples [31, 54–56] is provided in Table S15. The comparison includes CIE 1931 (x, y) colour coordinates of white emission, CIE 1931 (Δx, Δy) colour coordinate differences of emission at different electrical excitations, CRI, PE, EQE, and specific emission characteristics. The results demonstrate that compounds **4a**–**c** exhibit competitive white-light-emission performance with rather high colour stability while simultaneously combining mechanochromic behaviour, aggregation-enhanced emission, colour tunability, and successful implementation in down-converting white-light devices. In particular, device C based on **4c** achieves a PE of 10.8 lm W^{-1} with stable white-light emission (Δx of 0.008, Δy of 0.006), while all devices exhibit CRI values of 75–78 and CIE coordinates close to the white-light region. This highlights the potential of these materials as multifunctional single-component emitters for advanced optical and human-centric lighting applications, enabling single-molecular white emissions with stable colours at different voltages (Table S15).

3 | Conclusion

This study introduces novel pure organic single-molecular white-light emitters with solid-state-enhanced mechanochromic thermally activated delayed fluorescence, achieving significant emission enhancement and multicolor tunability through a strategic balance of phenothiazine moieties and a 3,5-dicyanopyridine core. The emitters exhibit significant solid-state

21951071, 2026, 35, Downloaded from https://advanced.onlinelibrary.wiley.com/doi/10.1002/adom.71715 by Dmytro Volyniuk - Kaunas University Of Technology , Wiley Online Library on [03/11/2026]. See the Terms and Conditions (https://onlinelibrary.wiley.com/terms-and-conditions) on Wiley Online Library for rules of use; OA articles are governed by the applicable Creative Commons License

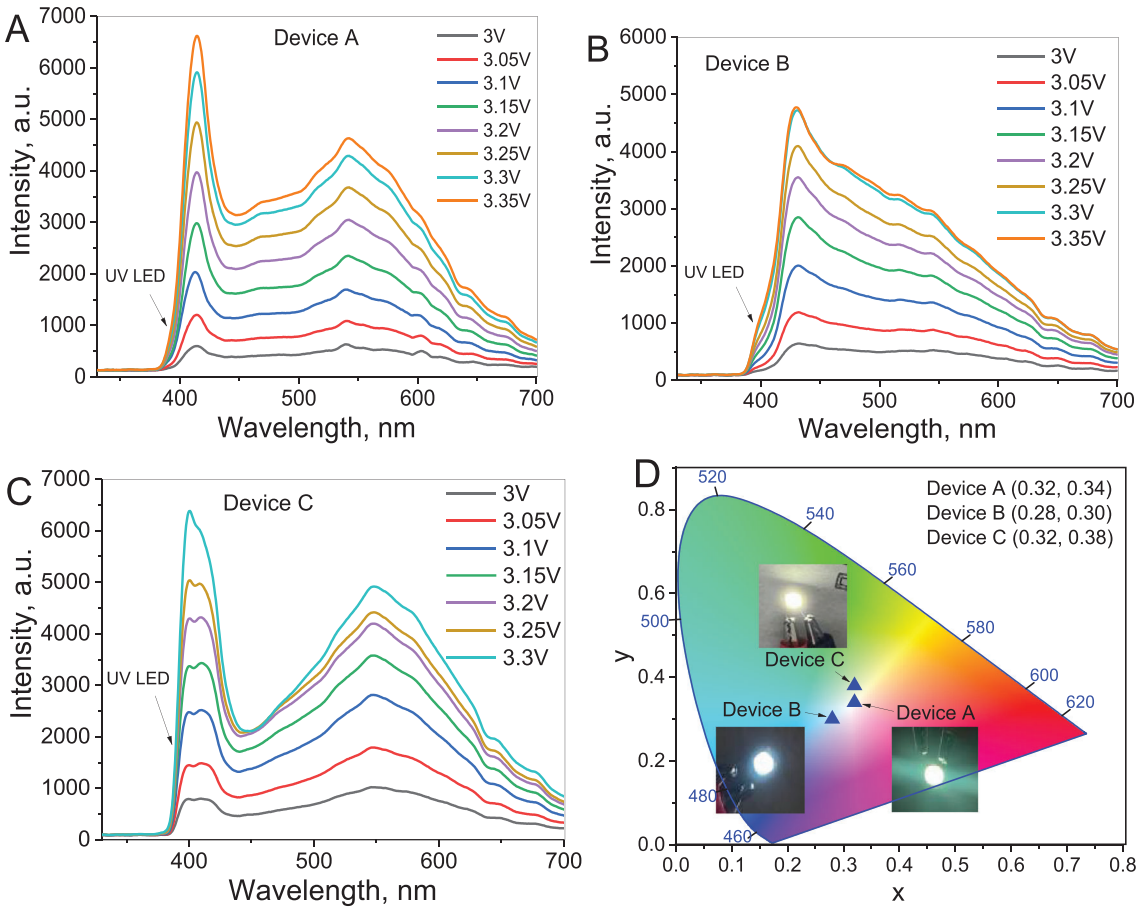


FIGURE 8 | EL spectra (A–C) of down-converting white light-emitting diodes A (A), B (B), and C (C) containing emitters **4a–c** recorded at the different voltages, the CIE1931 colour diagram with colour coordinates estimated at 3.1 V (D). The insets show photos of the devices taken at 3.1 V.

emission enhancement factors of up to 755, and the tunable multicolor emission arises from photoluminescence, response to physical treatments, and conformational arrangements in the solid state. The synthesized emitters produce white light with CIE 1931 coordinates close to (0.33, 0.33), facilitated by double photoluminescence bands and conformational flexibility in solid states. This makes them a promising alternative to conventional multicomponent systems. The compounds exhibit high thermal stability, with a 5% weight loss up to 422°C, ensuring long lifetimes in potential applications. They have different conformational states that enable emission ranging from deep blue to red. The crystalline forms support white or multicolor emissions, while amorphous states provide single-color outputs. X-ray analysis emphasizes the decisive influence of the planarity of the pyridine ring, the molecular packing, and π-hole, CH···N, CH···F, and CH···Br interactions. The observed PL decay rates for prompt fluorescence and TADF of different conformers are in agreement with the results of the DFT/TDDFT calculations. These advancements enable these compounds to function as single-molecular white-light emitters with sufficient white colour quality in single-emitter-based down-converting light-emitting diodes. The results pave the way for future research into organic single-molecular white emitters for down-converting electroluminescence with optimised efficiency and expanded application possibilities, with a focus on human-centric lighting applications.

4 | Experimental

4.1 | General Method for the Synthesis of 2,6-di(10H-Phenothiazin-10-yl) Substituted 3,5-Dicarbonitriles 4a–c

To a solution of 10*H*-phenothiazine (0.42 g, 2.1 mmol, 2.1 equiv.) in dry THF (5 mL) and DMF (2 mL) was added sodium hydride (60% in oil, 77.3 mg, 2.3 mmol, 2.3 equiv.) under argon and the mixture was stirred at 60°C for 3 h. Then appropriate 2,6- dibromide **3a–c** (1 mmol, 1 equiv.) was added in one portion and the mixture was stirred at 60°C overnight. After cooling the mixture was poured into water (40 mL) and the precipitates were filtered off. The crude product was purified by flash chromatography on silica gel with DCM/petroleum ether, 1:1→4:1 yielding white to light yellow powders.

4.1.1 | 4-Phenyl-2,6-di(10*H*-phenothiazin-10-yl) pyridine-3,5-dicarbonitrile (4a)

Yield: 426 mg (71%); Mp> 200°C. IR ν_{max} (film): 2214, 1541, 1477. ^{1}H NMR (400 MHz, Chloroform-*d*): 7.58–7.51 (m, 8H), 7.41 (dd, J = 6.7, 1.3 Hz, 3H), 7.34–7.27 (m, 10H). ^{13}C NMR (101 MHz, Chloroform- *d*): 164.8, 157.1, 140.5, 135.3, 134.4, 130.7, 129.3, 128.8,

21951071, 2026, 35, Downloaded from https://advanced.onlinelibrary.wiley.com/doi/10.1002/adom.71715 by Dmytro Volyniuk - Kaunas University Of Technology , Wiley Online Library on [03/11/2026]. See the Terms and Conditions (https://onlinelibrary.wiley.com/terms-and-conditions) on Wiley Online Library for rules of use; OA articles are governed by the applicable Creative Commons License

128.8, 127.7, 127.2, 127.1, 113.8, 87.5. HRMS: $[M+H]^+$ calcd for $C_{37}H_{22}N_5S_2^+$ 600.1317, found 600.1316. (V-P-74).

4.1.2 | 4-(4-Fluorophenyl)-2,6-di(10*H*-phenothiazin-10-yl)pyridine-3,5-dicarbonitrile (4b)

Yield: 402 mg (65%); Mp> 200°C. IR ν_{max} (film): 2210, 1598, 1542. ^{1}H NMR (400 MHz, Chloroform-*d*): 7.61–7.46 (m, 8H), 7.38–7.26 (m, 10H), 7.16–7.02 (m, 2H). ^{13}C NMR (101 MHz, Chloroform-*d*): 165.3, 163.7, 162.8, 157.1, 140.4, 135.4, 131.6 (d, J = 9.1 Hz), 130.4 (d, J = 3.0 Hz), 128.9, 127.7, 127.2 (d, J = 11.1 Hz), 116.1 (d, J = 22.2 Hz), 113.8, 87.3. ^{19}F NMR (376 MHz, $CDCl_3$) δ −109.03 – −109.1 (1F, m). HRMS: $[M+H]^+$ calcd for $C_{37}H_{21}FN_5S_2^+$ 618.1222, found: 618.1249. (V-P-73).

4.1.3 | 4-(4-Bromophenyl)-2,6-di(10*H*-phenothiazin-10-yl)pyridine-3,5-dicarbonitrile (4c)

Yield: 468 mg (69%); Mp> 200°C. IR ν_{max} (film): 2217, 1590, 1543. ^{1}H NMR (400 MHz, Chloroform-*d*): 7.57–7.50 (m, 10H), 7.36–7.27 (m, 8H), 7.21–7.14 (m, 2H). ^{13}C NMR (101 MHz, Chloroform-*d*): 163.6, 157.0, 140.3, 135.4, 133.3, 132.2, 130.9, 128.9, 127.7, 127.3, 127.2, 125.4, 113.6, 87.1. HRMS: $[M+H]^+$ calcd for $C_{37}H_{21}BrN_5S_2^+$ 678.0422, found 678.0408. (V-P-79).

4.2 | Single Crystal Analyses

Single crystals of **4b** (with sizes 0.16 × 0.12 × 0.03 mm^3) and **4c** (with sizes 0.13 × 0.08 × 0.02 mm^3) were investigated on a Rigaku, XtaLAB Synergy, Dualflex, HyPix diffractometer at different temperatures using monochromated CuKα radiation (λ = 1.54184 Å). For further details, see crystallographic data for these compounds deposited at the Cambridge Crystallographic Data Centre as Supplementary Publications with the corresponding CCDC deposition numbers (https://www.ccdc.cam.ac.uk/services/structures). These data are provided free of charge by the joint Cambridge Crystallographic Data Centre and Fachinformationszentrum Karlsruhe Access Structures service [CCDC for **4b**: 2358532 (at 150 K), 2358541 (at 273 K), 2358540 (at 363 K); for **4c**: 2358562 (at 160 K), 2358563 (at 273 K)].

4.3 | Computational Details

The density functional theory (DFT) and time-dependent (TD) DFT calculations were implemented within the Gaussian 16 (Revision A.03) software package [57]. The ground singlet state, excited singlet (S_1), and triplet (T_1) state geometries were calculated using the long-range corrected ωB97XD functional, [58, 59] which incorporates long-range corrections (ωB97) and empirical dispersion (XD) corrections using Grimme's D2 dispersion model [60]. The 6–31G(d,p) basis set [61, 62] was used for all DFT and TDDFT calculations [59–61]. The B3LYP functional [63, 64] and the 6–31G(d,p) basis set were employed for vertical absorption spectra calculations, starting from the ωB97XD/6-31G(d,p) optimized geometry. The polarizable continuum model (PCM) with the integral equation formalism (IEF) was used to simulate the solvent effect, taking tetrahydrofuran (THF, ε = 7.43) as a model solvent [65–67]. The TDDFT calculations using the ωB97XD functional show a blue shift (up to 20–40 nm) of the absorption bands **4a–c** relative to the B3LYP reference. Similar blueshifts of CT absorption bands upon implementation of the long-range corrected functionals have been widely reported for donor-acceptor systems, reflecting the improved treatment of long-range exchange in TDDFT calculations [68–71]. No imaginary frequencies indicating the presence of a saddle point on the potential energy surface were found for any of the optimized structures of the studied molecular conformations 1–3 of **4a–c**.

4.4 | Photophysical Experiments

Edinburgh Instruments spectrometer FLS980 and Avantes AvaSpec-2048XL spectrometer were used to record the emission and UV/vis absorption spectra of compounds **4a–c**, respectively. Low-temperature (77 K) phosphorescence spectra were collected with a delay time of 1 ms following excitation. Photoluminescence decay profiles were measured using a PicoQuant LDH-D-C-375 laser (at 374 nm) as the excitation source. The photoluminescence quantum yields (PLQYs) were estimated using an integrated sphere with a 120 mm inner diameter connected to the FLS980 spectrometer.

4.5 | Powder X-Ray Diffraction Study

D8 Discover X-ray diffractometer (Bruker AXS GmbH) with a Cu K_α (λ = 1.54 Å) X-ray source was used to record X-ray diffractograms of the powders of **4a–c**. We used parallel beam geometry with a 60 mm Göbel mirror (i.e., X-ray mirror on a high precision parabolic surface). The primary side also had a Soller slit with an axial divergence of 2.5 ° and a slit of 1.0 mm. The secondary side had a LYNXEYE (1D mode) detector with an opening angle of 2.16 ° and a slit opening of 6.0 mm. X-ray generator voltage and current were 40.0 kV and 40 mA, respectively. Coupled $2\theta/\theta$ scans were performed in the range of 5.0°–90.0° with a step size of 0.043°, time per step of 19.2 s, and auto-repeat function enabled. Processing of the resultant diffractograms was performed with DIFFRAC.EVA software. For the X-ray diffraction measurements at grazing incidence (XRDGI), the scans were performed at an incidence angle of 1.50°. Crystallinity was calculated using formulas (1) and (2):

$$\%\text{Amorphous} = \frac{\text{Global area} - \text{Area under Bragg Reflections}}{\text{Global area}} * 100\% \quad (1)$$

$$\%\text{Crystallinity} = 100\% - \%\text{Amorphous} \quad (2)$$

4.6 | Thermal Study

Thermogravimetric analysis (TGA) was undertaken on a TA Instruments TGA Q50 apparatus by recording the weight loss during heating from 0 to 800°C at the rate of 20°C min^{-1} under a nitrogen atmosphere of 50 mL min^{-1}. TA Instruments DSC Q2000 equipment was used for differential scanning calorimetry (DSC) measurements at heating and cooling rates of 10°C/min under N_2

21951071, 2026, 35, Downloaded from https://advanced.onlinelibrary.wiley.com/doi/10.1002/adom.71715 by Dmytro Volyniuk - Kaunas University Of Technology , Wiley Online Library on [03/11/2026]. See the Terms and Conditions (https://onlinelibrary.wiley.com/terms-and-conditions) on Wiley Online Library for rules of use; OA articles are governed by the applicable Creative Commons License

flow of 40 mL min^{-1} with an empty aluminium pan taken as a standard.

4.7 | Down-Converting Light-Emitting Diodes

The films were cast onto bare UV LEDs from highly concentrated toluene solutions of inert-polymer-matrix Zeonex (100 mg/ml). These Zeonex solutions contained dispersions of white-emitting powders of **4a–c**, which were only partially dissolved in toluene. The Zeonex-to-emitter ratio was 100:1. Before the deposition of white-emitting films, the toluene dispersions of Zeonex and of **4a–c** were mixed in an ultrasonic bath for 30 min. The thicknesses of down-converting white-emitting films of the dispersions of **4a–c** in Zeonex were optimized for the reduction of the EL intensity of the UV LED. The fabricated down-converting light-emitting diodes were characterised using a multi-source meter (Keithley 2400), a spectrometer (Avantes AvaSpec-2048XL), a certified photodiode (PH100-Si-HA-D0) operated via the PC-Based Power and Energy Monitor 11S-LINK (from STANDA), and a computer equipped with the relevant software. The colour parameters CIE1931, CRI, and T_C were estimated using the emission spectra of the devices recorded at the different voltages.

Author Contributions

Lesia Volyniuk: Investigation, data curation, formal analysis, Visualization; **Brigita Vigante**: Investigation, data curation, formal analysis; **Dmytro Volyniuk**: Conceptualization, writing – original draft, investigation, supervision, methodology, funding acquisition; **Nataliya M. Karaush-Karmazin**: Writing – original draft, investigation, **Boris F. Minaev:** Writing – review & editing, investigation, methodology, validation; **Serhii Melnykov**: Investigation, data curation; visualization; **Pavlo Stakhira**: Investigation, unding acquisition; **Algirdas Lazauskas**: Investigation, data curation; **Sergey Belyakov**: Investigation, data curation, formal analysis, co-writing – original draft; **Santhiya Kuppusamy**: Investigation; **Pavel Arsenyan**: Conceptualization, writing – original draft, investigation, supervision, methodology, funding acquisition, validation, visualization; **Juozas Vidas Grazulevicius**: Writing – review & editing, validation, supervision, funding acquisition.

Acknowledgements

This project has received funding from the Research Council of Lithuania (LMTLT), project COLED, agreement No S-MIP-24-2 and by the National Science Foundation of Ukraine (NSFU) (Grant No 0124U003833). This work is also supported by Horizon Europe, the European Union's framework programme for research and innovation (R&I) for 2021–2027, project HELIOS, grant agreement No 101155017. The quantum-chemical calculations were carried out by N.K.-K. using computational resources provided by the National Academic Infrastructure for Supercomputing in Sweden (NAISS 2025-5-140) at the National Supercomputer Centre (NSC), Linköping University, partially funded by the Swedish Research Council (Grant Number. 2022–06725).

Funding

This project has received funding from the Research Council of Lithuania (LMTLT), project COLED, agreement No S-MIP-24-2. This work is also supported by Horizon Europe, the European Union's framework programme for research and innovation (R&I) for 2021–2027, project HELIOS, grant agreement No 101155017. The quantum-chemical calculations were carried out by N.K.-K. using computational resources provided by the National Academic Infrastructure for Supercomputing in Sweden (NAISS 2025-5-140) at the National Supercomputer Centre (NSC), Linköping University, partially funded by the Swedish Research Council (grant no. 2022–06725).

Conflicts of Interest

The authors declare no conflicts of interest.

Data Availability Statement

The data that support the findings of this study are available in the published article and its Supporting Information. Additional raw data are available from the corresponding author upon reasonable request. [CCDC for **4b**: 2358532 (at 150 K), 2358541 (at 273 K), 2358540 (at 363 K); for **4c**: 2358562 (at 160 K), 2358563 (at 273 K) contains the supplementary crystallographic data for this paper. These data can be obtained free of charge from The Cambridge Crystallographic Data Centre via www.ccdc.cam.ac.uk/data_request/cif].

References

1. Z. Chen, C. L. Ho, L. Wang, and W. Y. Wong, "Single-Molecular White-Light Emitters and Their Potential WOLED Applications," *Advanced Materials* 32 (2020): 201903269, https://doi.org/10.1002/adma.201903269.

2. N. J. Findlay, J. Bruckbauer, A. R. Inigo, et al., "An Organic Down-Converting Material for White-Light Emission from Hybrid LEDs," *Advanced Materials* 26 (2014): 1402661.

3. J. Ajantha, P. Yuvaraj, M. Karuppusamy, and S. Easwaramoorthi, "Single-Molecule White-Light-Emitting Starburst Donor-Acceptor Triphenylamine Derivatives and Their Application as Ratiometric Luminescent Molecular Thermometers," *Chemistry—A European Journal* 27 (2021): 11319–11325, https://doi.org/10.1002/chem.202100748.

4. S. Dey, R. Deka, M. Upadhyay, S. Peethambaran, and D. Ray, "White Light Emission via Dual Thermally Activated Delayed Fluorescence From a Single-Component Phenothiazines–Diphenyl Quinoline Conjugate," *The Journal of Physical Chemistry Letters* 15 (2024): 3135–3141, https://doi.org/10.1021/acs.jpclett.4c00185.

5. M. T. Sajjad, P. P. Manousiadis, H. Chun, et al., "Novel Fast Color-Converter for Visible Light Communication Using a Blend of Conjugated Polymers," *ACS Photonics* 2 (2015): 194–199, https://doi.org/10.1021/ph500451y.

6. K. Guo, Z. Tang, X. Chou, et al., "Printable Organic Light-Emitting Diodes for Next-Generation Visible Light Communications: A Review," *Advanced Photonics Nexus* 2 (2023): 044001, https://doi.org/10.1117/1.APN.2.4.044001.

7. Y. Liang, P. Hu, H. Zhang, et al., "Enabling Highly Robust Full-Color Ultralong Room-Temperature Phosphorescence and Stable White Organic Afterglow From Polycyclic Aromatic Hydrocarbons," *Angewandte Chemie International Edition* 63 (2024): 202318516, https://doi.org/10.1002/anie.202318516.

8. Y. Zhuang and R. J. Xie, "Mechanoluminescence Rebrightening the Prospects of Stress Sensing: A Review," *Advanced Materials* 33 (2021): 2005925, https://doi.org/10.1002/adma.202005925.

9. R. Varghese and H. A. Wagenknecht, "White-Light-Emitting DNA (WED)," *Chemistry—A European Journal* 15 (2009): 9307–9310, https://doi.org/10.1002/chem.200901147.

10. B. Roy, M. C. Reddy, G. P. Jose, F. C. Niemeyer, J. Voskuhl, and P. Hazra, "All in One: Stimuli-Responsive, Efficient Mitotracking, and Single Source White Light Emission," *The Journal of Physical Chemistry Letters* 12 (2021): 1162–1168, https://doi.org/10.1021/acs.jpclett.0c03489.

11. G. Li, M. Du, T. Fan, X. Luo, L. Duan, and Y. Zhang, "Asymmetric Structural Design of a Highly Oriented Multi-Resonance Emitter Enables a Record 41.5% External Quantum Efficiency in Deep-Blue OLED," *Materials Today* 73 (2024): 30–37, https://doi.org/10.1016/j.mattod.2024.01.003.

21951071, 2026, 35, Downloaded from https://advanced.onlinelibrary.wiley.com/doi/10.1002/adom.71715 by Dmytro Volyniuk - Kaunas University Of Technology , Wiley Online Library on [03/11/2026]. See the Terms and Conditions (https://onlinelibrary.wiley.com/terms-and-conditions) on Wiley Online Library for rules of use; OA articles are governed by the applicable Creative Commons License

12. L. Jia, L. Jin, K. Yuan, et al., "High-Performance Exciplex-Type Host for Multicolor Phosphorescent Organic Light-Emitting Diodes With Low Turn-On Voltages," *ACS Sustainable Chemistry & Engineering* 6 (2018): 8809–8815, https://doi.org/10.1021/acssuschemeng.8b01155.

13. M. Bachmann, D. Suter, O. Blacque, and K. Venkatesan, "Tunable and Efficient White Light Phosphorescent Emission Based on Single Component N-Heterocyclic Carbene Platinum(II) Complexes," *Inorganic Chemistry* 55 (2016): 4733–4745, https://doi.org/10.1021/acs.inorgchem.5b02962.

14. G. Li, T. Fleetham, and J. Li, "Efficient and Stable White Organic Light-Emitting Diodes Employing a Single Emitter," *Advanced Materials* 26 (2014): 2931–2936, https://doi.org/10.1002/adma.201305507.

15. M. Pan, W. M. Liao, S. Y. Yin, S. S. Sun, and C. Y. Su, "Single-Phase White-Light-Emitting and Photoluminescent Color-Tuning Coordination Assemblies," *Chemical Reviews* 118 (2018): 8889–8935, https://doi.org/10.1021/acs.chemrev.8b00222.

16. Z. Ma, X. Ji, M. Wang, et al., "Emerging New-Generation White Light-Emitting Diodes Based on Luminescent Lead-Free Halide Perovskites and Perovskite derivatives," *Nano Select* 3 (2022): 280–297, https://doi.org/10.1002/nano.202100059.

17. J. Zhang, X. Zhao, H. Shen, J. W. Y. Lam, H. Zhang, and B. Z. Tang, "White-Light Emission From Organic Aggregates: A Review," *Advanced Photonics* 4 (2021): 014001, https://doi.org/10.1117/1.AP.4.1.014001.

18. L. Volyniuk, D. Gudeika, A. A. Panchenko, et al., "Single-Molecular White Emission of Organic Thianthrene-Based Luminophores Exhibiting Efficient Fluorescence and Room Temperature Phosphorescence Induced by Halogen Atoms," *ACS Sustainable Chemistry & Engineering* 11 (2023): 16914–16925, https://doi.org/10.1021/acssuschemeng.3c04011.

19. H. Sun, M. He, and G. V. Baryshnikov, et al., "Engineering Tunable Ratiometric Dual Emission in Single Emitter-based Amorphous Systems," *Angewandte Chemie International Edition* 63 (2024): 202318159, https://doi.org/10.1002/anie.202318159.

20. N. A. Kukhta and M. R. Bryce, "Dual Emission in Purely Organic Materials for Optoelectronic Applications," *Materials Horizons* 8 (2021): 33–55, https://doi.org/10.1039/D0MH01316A.

21. J. Mei, N. L. C. Leung, R. T. K. Kwok, J. W. Y. Lam, and B. Z. Tang, "Aggregation-Induced Emission: Together We Shine, United We Soar!," *Chemical Reviews* 115 (2015): 11718–11940, https://doi.org/10.1021/acs.chemrev.5b00263.

22. Y. Sun, Z. Lei, and H. Ma, "Twisted Aggregation-Induced Emission Luminogens (AIEgens) Contribute to Mechanochromism Materials: A Review," *Journal of Materials Chemistry C* 10 (2022): 14834–14867, https://doi.org/10.1039/D2TC02512D.

23. Q. Li, Y. Wu, J. Cao, et al., "Pillararene-Induced Intramolecular Through-Space Charge Transfer and Single-Molecule White-Light Emission," *Angewandte Chemie* 134 (2022): 202202381, https://doi.org/10.1002/ange.202202381.

24. S. Hirata, "Recent Advances in Materials With Room-Temperature Phosphorescence: Photophysics for Triplet Exciton Stabilization," *Advanced Optical Materials* 5 (2017): 1700116, https://doi.org/10.1002/adom.201700116.

25. Y. Liu, C. Li, Z. Ren, S. Yan, and M. R. Bryce, "All-Organic Thermally Activated Delayed Fluorescence Materials for Organic Light-Emitting Diodes," *Nature Reviews Materials* 3 (2018): 18020, https://doi.org/10.1038/natrevmats.2018.20.

26. H. H. Cho, S. Gorgon, G. Londi, et al., "Efficient Near-Infrared Organic Light-Emitting Diodes With Emission from Spin Doublet Excitons," *Nature Photonics* 18 (2024): 905–912, https://doi.org/10.1038/s41566-024-01458-3.

27. O. Chatterjee, R. Roy, A. Pramanik, et al., "Dynamic Self-Assembly of Photo-Reduced Perylene Diimide: Single-Component White Light Emission From Organic Radicals," *Advanced Optical Materials* 10 (2022): 2201187, https://doi.org/10.1002/adom.202201187.

28. M. Stanitska, D. Volyniuk, B. Minaev, H. Agren, and J. V. Grazulevicius, "Molecular Design, Synthesis, Properties, and Applications of Organic Triplet Emitters Exhibiting Blue, Green, Red and White Room-Temperature Phosphorescence," *Journal of Materials Chemistry C* 12 (2024): 2662–2698, https://doi.org/10.1039/D3TC04514E.

29. Y. Zhang, Y. Miao, X. Song, et al., "Single-Molecule-Based White-Light Emissive Organic Solids With Molecular-Packing-Dependent Thermally Activated Delayed Fluorescence," *The Journal of Physical Chemistry Letters* 8 (2017): 4808–4813, https://doi.org/10.1021/acs.jpclett.7b02213.

30. J. Rui, J. Pu, Z. Chen, et al., "Single-Molecule White Organic Light-Emitting Diodes Based on Dual-Conformation Diindolophenthiazine Derivatives," *Journal of Materials Chemistry C* 12 (2024): 9182–9188, https://doi.org/10.1039/D4TC01203H.

31. M. Liu, H. Hao, G. Liao, et al., "Boron-Containing Molecules With Fluorescence-Phosphorescence Dual-Emission for Mechanochromism and Single Molecular White Light-Emitting Diodes," *Advanced Optical Materials* 11 (2023): 2202918, https://doi.org/10.1002/adom.202202918.

32. Z. Xie, C. Chen, S. Xu, et al., "White-Light Emission Strategy of a Single Organic Compound With Aggregation-Induced Emission and Delayed Fluorescence Properties," *Angewandte Chemie International Edition* 54 (2015): 7181–7184, https://doi.org/10.1002/anie.201502180.

33. Y. Huang, L. Ning, X. Zhang, Q. Zhou, Q. Gong, and Q. Zhang, "Stimuli-Fluorochromic Smart Organic Materials," *Chemical Society Reviews* 53 (2024): 1090–1166, https://doi.org/10.1039/D2CS00976E.

34. Y. Sagara, S. Yamane, M. Mitani, C. Weder, and T. Kato, "Mechanoresponsive Luminescent Molecular Assemblies: An Emerging Class of Materials," *Advanced Materials* 28 (2016): 1073–1095, https://doi.org/10.1002/adma.201502589.

35. W. Yang, Y. Yang, X. Cao, et al., "On-Off Switchable Thermally Activated Delayed Fluorescence Controlled by Multiple Channels: Understanding the Mechanism Behind Distinctive Polymorph-Dependent Optical Properties," *Chemical Engineering Journal* 415 (2021): 128909, https://doi.org/10.1016/j.cej.2021.128909.

36. F. Khan and R. Misra, "Recent advances in the development of phenothiazine and its fluorescent derivatives for optoelectronic applications," *Journal of Materials Chemistry C* 11 (2023): 2786–2825, https://doi.org/10.1039/D2TC04326B.

37. R. Pashazadeh, G. Sych, S. Nasiri, et al., "Multifunctional Asymmetric D-A-D′ Compounds: Mechanochromic Luminescence, Thermally Activated Delayed Fluorescence and Aggregation Enhanced Emission," *Chemical Engineering Journal* 401 (2020): 125962, https://doi.org/10.1016/j.cej.2020.125962.

38. M. Guzauskas, D. Volyniuk, I. Kulszewicz-Bajer, et al., "Thermally Controllable Tuning of Emission Properties of Phenoxazine-Substituted Acridones as One Step Forward to Efficient Organic Light-Emitting Diodes Based on Crystalline Emitters," *Advanced Optical Materials* 11 (2023): 2301059, https://doi.org/10.1002/adom.202301059.

39. G. Sych, R. Pashazadeh, Y. Danyliv, et al., "Reversibly Switchable Phase-Dependent Emission of Quinoline and Phenothiazine Derivatives towards Applications in Optical Sensing and Information Multicoding," *Chemistry—A European Journal* 27 (2021): 2826–2836, https://doi.org/10.1002/chem.202004657.

40. M. Okazaki, Y. Takeda, P. Data, et al., "Thermally Activated Delayed Fluorescent Phenothiazine–Dibenzo[a,j]Phenazine–Phenothiazine Triads Exhibiting Tricolor-Changing Mechanochromic Luminescence," *Chemical Science* 8 (2017): 2677–2686, https://doi.org/10.1039/C6SC04863C.

41. B. Vigante, K. Leitonas, D. Volyniuk, et al., "Synthesis of Linear and V-Shaped Carbazolyl-Substituted Pyridine-3,5-dicarbonitriles Exhibiting Efficient Bipolar Charge Transport and E-Type Fluorescence," *Chemistry—A European Journal* 25 (2019): 3325–3336, https://doi.org/10.1002/chem.201805323.

42. P. Arsenyan, B. Vigante, K. Leitonas, et al., "Dual Versus Normal TADF of Pyridines Ornamented With Multiple Donor Moieties and Their

21951071, 2026, 35, Downloaded from https://advanced.onlinelibrary.wiley.com/doi/10.1002/adom.71715 by Dmytro Volyniuk - Kaunas University Of Technology , Wiley Online Library on [03/11/2026]. See the Terms and Conditions (https://onlinelibrary.wiley.com/terms-and-conditions) on Wiley Online Library for rules of use; OA articles are governed by the applicable Creative Commons License

Performance in OLEDs," *Journal of Materials Chemistry C* 9 (2021): 3928–3938, https://doi.org/10.1039/D0TC05745B.

43. K. Leitonas, B. Vigante, D. Volyniuk, et al., "11,3,5-Dicyanopyridine Motifs for Electron-Transporting Semiconductors: From Design and Synthesis to Efficient Organic Light-Emitting Diodes," *Journal of Materials Chemistry C* 11 (2023): 9514–9526, https://doi.org/10.1039/D3TC00841J.

44. M. Ferreira, N. O. Decarli, A. Nyga, et al., "Multifunctional Tris(triazolo)Triazine-Based Emitter With Dual-TADF, RTP, AIEE and AIDF Properties," *Journal of Materials Chemistry C* 12 (2024): 13651–13664, https://doi.org/10.1039/D4TC00606B.

45. B. Kumari, R. Dahiwadkar, and S. Kanvah, "White Light Emission From AIE-Active Luminescent Organic Materials," *Aggregate* 3 (2022): 191, https://doi.org/10.1002/agt2.191.

46. J. Daub, R. Engl, J. Kurzawa, et al., "Competition Between Conformational Relaxation and Intramolecular Electron Transfer Within Phenothiazine–Pyrene Dyads," *The Journal of Physical Chemistry A* 105 (2001): 5655–5665, https://doi.org/10.1021/jp0037293.

47. J. Yang, J. Qin, P. Geng, J. Wang, M. Fang, and Z. Li, "Molecular Conformation-Dependent Mechanoluminescence: Same Mechanical Stimulus but Different Emissive Color Over Time," *Angewandte Chemie* 130 (2018): 14370–14374, https://doi.org/10.1002/ange.201809463.

48. M. Gao, Y. Tian, X. Li, et al., "The Effect of Molecular Conformations and Simulated "Self-Doping" in Phenothiazine Derivatives on Room-Temperature Phosphorescence," *Angewandte Chemie* 135 (2023): 202214908, https://doi.org/10.1002/ange.202214908.

49. F. Khan, A. Ekbote, G. Singh, and R. Misra, "Mechanochromic Luminogens With Hypsochromically Shifted Emission Switching Property: Recent Advances and Perspectives," *Journal of Materials Chemistry C* 10 (2022): 5024–5064, https://doi.org/10.1039/D1TC06140B.

50. F. Oroojalian, F. Azizollahi, P. Kesharwani, and A. Sahebkar, "Stimuli-Responsive Nanotheranostic Systems Conjugated With AIEgens for Advanced Cancer Bio-Imaging and Treatment," *Journal of Controlled Release* 373 (2024): 766–802, https://doi.org/10.1016/j.jconrel.2024.07.048.

51. P. Galer, R. C. Korošec, M. Vidmar, and B. Šket, "Crystal Structures and Emission Properties of the BF_2 Complex 1-phenyl-3-(3,5-Dimethoxyphenyl)-Propane-1,3-Dione: Multiple Chromisms, Aggregation- or Crystallization-Induced Emission, and the Self-Assembly Effect," *Journal of the American Chemical Society* 136 (2014): 7383–7394, https://doi.org/10.1021/ja501977a.

52. R. Sharma, D. Volyniuk, C. Popli, O. Bezvikonnyi, J. V. Grazulevicius, and R. Misra, "Strategy Toward Tuning Emission of Star-Shaped Tetraphenylethene-Substituted Truxenes for Sky-Blue and Greenish-White Organic Light-Emitting Diodes," *The Journal of Physical Chemistry C* 122 (2018): 15614–15624, https://doi.org/10.1021/acs.jpcc.8b00777.

53. M. Yamazaki, "Industrialization and Application Development of Cyclo-Olefin Polymer," *Journal of Molecular Catalysis A: Chemical* 213 (2004): 81–87, https://doi.org/10.1016/j.molcata.2003.10.058.

54. J. Rui, J. Pu, Z. Chen, et al., "Single-Molecule White Organic Light-Emitting Diodes Based on Dual-Conformation Diindolophenthiazine Derivatives," *Journal of Materials Chemistry C* 12 (2024): 9182–9188, https://doi.org/10.1039/D4TC01203H.

55. M. Zhang, W. Li, S.-W. Zhang, et al., "Efficient Single-Molecular White-Light Emission for Iridium-Based Photoluminescent and Electroluminescent White OLEDs," *Cell Reports Physical Science* 4 (2023): 101684, https://doi.org/10.1016/j.xcrp.2023.101684.

56. M. Liu, H. Li, H. Ma, et al., "Triarylboron-Based Dual Thermally Activated Delayed Fluorescence Emitter for Single Molecule White Light-Emitting Diodes," *ACS Applied Materials & Interfaces* 17 (2025): 21509–21520, https://doi.org/10.1021/acsami.4c20583.

57. H. B. Schlegel, G. E. Scuseria, M. A. Robb, et al., *Gaussian 09, Revision A.02′ Inc* (Gaussian Inc, 2009).

58. J. D. Chai and M. Head-Gordon, "Long-Range Corrected Hybrid Density Functionals With Damped Atom–Atom Dispersion Corrections," *Physical Chemistry Chemical Physics* 10 (2008): 6615–6620, https://doi.org/10.1039/B810189B.

59. J. D. Chai and M. Head-Gordon, "Systematic Optimization of Long-Range Corrected Hybrid Density Functionals," *The Journal of Chemical Physics* 128 (2008): 084106, https://doi.org/10.1063/1.2834918.

60. S. Grimme, J. Antony, S. Ehrlich, and H. Krieg, "A Consistent and Accurate Ab Initio Parametrization of Density Functional Dispersion Correction (DFT-D) for the 94 Elements H-Pu," *The Journal of Chemical Physics* 132 (2010): 154104, https://doi.org/10.1063/1.3382344.

61. M. Frisch, J. Pople, and S. Binkley, "Self-Consistent Molecular Orbital Methods 25. Supplementary Functions for Gaussian Basis Sets," *The Journal of Chemical Physics* 80 (1984): 3265–3269, https://doi.org/10.1063/1.447079.

62. M. M. Francl, W. J. Pietro, W. J. Hehre, et al., "Self-Consistent Molecular Orbital Methods. XXIII. A Polarization-Type Basis Set for Second-Row Elements," *The Journal of Chemical Physics* 77 (1982): 3654–3665, https://doi.org/10.1063/1.444267.

63. E. Runge and E. K. U. Gross, "Density-Functional Theory for Time-Dependent Systems," *Physical Review Letters* 52 (1984): 997–1000, https://doi.org/10.1103/PhysRevLett.52.997.

64. S. Miertuš, E. Scrocco, and J. Tomasi, "Electrostatic Interaction of a Solute With a Continuum. A Direct Utilizaion of AB Initio Molecular Potentials for the Prevision of Solvent Effects," *Chemical Physics* 55 (1981): 117–129, https://doi.org/10.1016/0301-0104(81)85090-2.

65. A. D. Becke, "Perspective: Fifty Years of Density-Functional Theory in Chemical Physics," *The Journal of Chemical Physics* 140 (2014): 18A301, https://doi.org/10.1063/1.4869598.

66. A. D. Becke, "Density-Functional Thermochemistry. III. The Role of Exact Exchange," *The Journal of Chemical Physics* 98 (1993): 5648–5652, https://doi.org/10.1063/1.464913.

67. C. Lee, W. Yang, and R. G. Parr, "Development of the Colle-Salvetti Correlation-Energy Formula Into a Functional of the Electron Density," *Physical Review B* 37 (1988): 785–789, https://doi.org/10.1103/PhysRevB.37.785.

68. E. Cancès and B. Mennucci, "New Applications of Integral Equations Methods for Solvation Continuum Models: Ionic Solutions and Liquid Crystals," *Journal of Mathematical Chemistry* 23 (1998): 309–326, https://doi.org/10.1023/A:1019133611148.

69. E. Cancès, B. Mennucci, and J. Tomasi, "A New Integral Equation Formalism for the Polarizable Continuum Model: Theoretical Background and Applications to Isotropic and Anisotropic Dielectrics," *The Journal of Chemical Physics* 107 (1997): 3032–3041, https://doi.org/10.1063/1.474659.

70. B. Mennucci, E. Cancès, and J. Tomasi, "Evaluation of Solvent Effects in Isotropic and Anisotropic Dielectrics and in Ionic Solutions With a Unified Integral Equation Method: Theoretical Bases, Computational Implementation, and Numerical Applications," *The Journal of Physical Chemistry B* 101 (1997): 10506–10517, https://doi.org/10.1021/jp971959k.

71. J. Tomasi, B. Mennucci, and R. Cammi, "Quantum Mechanical Continuum Solvation Models," *Chemical Reviews* 105 (2005): 2999–3094, https://doi.org/10.1021/cr9904009.

Supporting Information

Additional supporting information can be found online in the Supporting Information section.

Supporting File: adom71715-sup-0001-SuppMat.pdf.

21951071, 2026, 35, Downloaded from https://advanced.onlinelibrary.wiley.com/doi/10.1002/adom.71715 by Dmytro Volyniuk - Kaunas University Of Technology , Wiley Online Library on [03/11/2026]. See the Terms and Conditions (https://onlinelibrary.wiley.com/terms-and-conditions) on Wiley Online Library for rules of use; OA articles are governed by the applicable Creative Commons License